

Tumor-targeted delivery of hyaluronic acid/polydopamine-coated Fe²⁺-doped nano-scaled metal–organic frameworks with doxorubicin payload for glutathione depletion-amplified chemodynamic-chemo cancer therapy

Kai-An Liang^a, Hsiang-Yun Chih^a, I-Ju Liu^a, Nien-Tzu Yeh^a, Tsai-Ching Hsu^{b,c,d}, Hao-Yang Chin^b, Bor-Show Tzang^{b,c,d,e,*}, Wen-Hsuan Chiang^{a,**}

^a Department of Chemical Engineering, i-Center for Advanced Science and Technology (iCAST), National Chung Hsing University, Taichung 402, Taiwan

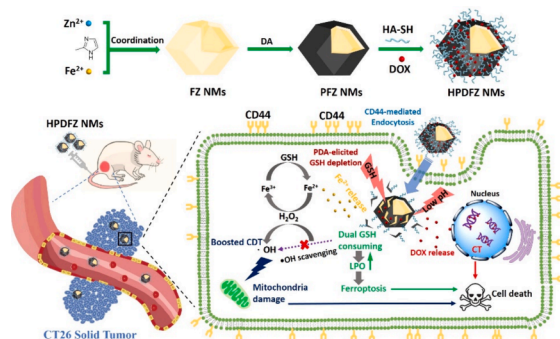
^b Institute of Medicine, Chung Shan Medical University, Taichung 402, Taiwan

^c Immunology Research Center, Chung Shan Medical University, Taichung 402, Taiwan

^d Department of Clinical Laboratory, Chung Shan Medical University Hospital, Taichung 402, Taiwan

^e Department of Biochemistry, School of Medicine, Chung Shan Medical University, Taichung 402, Taiwan

GRAPHICAL ABSTRACT



ARTICLE INFO

Keywords:
NanoMOFs
dual GSH depletion
Chemodynamic-chemo therapy
Active tumor targeting
Hyaluronic acid

ABSTRACT

Chemodynamic therapy (CDT), an emerging cancer treatment modality, uses multivalent metal elements to convert endogenous hydrogen peroxide (H₂O₂) to toxic hydroxyl radicals (•OH) via a Fenton or Fenton-like reaction, thus eliciting oxidative damage of cancer cells. However, the antitumor potency of CDT is largely limited by the high glutathione (GSH) concentration and low catalytic efficiency in the tumor sites. The combination of CDT with chemotherapy provides a promising strategy to overcome these limitations. In this work, to enhance antitumor potency by tumor-targeted and GSH depletion-amplified chemodynamic-chemo therapy, the hyaluronic acid (HA)/polydopamine (PDA)-decorated Fe²⁺-doped ZIF-8 nano-scaled metal–organic frameworks

* Corresponding author at: Institute of Medicine, Chung Shan Medical University, Taichung 402, Taiwan.

** Corresponding author at: Department of Chemical Engineering, i-Center for Advanced Science and Technology (iCAST), National Chung Hsing University, Taichung 402, Taiwan.

E-mail addresses: bstzang@csmu.edu.tw (B.-S. Tzang), whchiang@dragon.nchu.edu.tw (W.-H. Chiang).

<https://doi.org/10.1016/j.jcis.2024.07.241>

Received 4 June 2024; Received in revised form 27 July 2024; Accepted 30 July 2024

Available online 31 July 2024

0021-9797/© 2024 Elsevier Inc. All rights are reserved, including those for text and data mining, AI training, and similar technologies.

(FZ NMs) were fabricated and utilized to load doxorubicin (DOX), a chemotherapy drug, via hydrophobic, π - π stacking and charge interactions. The attained HA/PDA-covered DOX-carrying FZ NMs (HPDFZ NMs) promoted DOX and Fe^{2+} release in weakly acidic and GSH-rich milieu and exhibited acidity-activated $\bullet\text{OH}$ generation. Through efficient CD44-mediated endocytosis, the HPDFZ NMs internalized by CT26 cells not only prominently enhanced $\bullet\text{OH}$ accumulation by consuming GSH via PDA-mediated Michael addition combined with $\text{Fe}^{2+}/\text{Fe}^{3+}$ redox couple to cause mitochondria damage and lipid peroxidation, but also achieved intracellular DOX release, thus eliciting apoptosis and ferroptosis. Importantly, the HPDFZ NMs potently inhibited CT26 tumor growth in vivo at a low DOX dose and had good biosafety, thereby showing promising potential in tumor-specific treatment.

1. Introduction

Chemodynamic therapy (CDT) is an innovative tumor-specific catalytic treatment that utilizes transition metal ions (e.g., $\text{Fe}^{2+}/\text{Fe}^{3+}$, $\text{Cu}^+/\text{Cu}^{2+}$, and $\text{Mn}^{2+}/\text{Mn}^{3+}$) to convert hydrogen peroxide (H_2O_2) overexpressed in the tumor site to toxic hydroxyl radicals ($\bullet\text{OH}$) via Fenton/Fenton-like reaction [1–7]. The overproduction of intracellular $\bullet\text{OH}$ can lead to lipid peroxidation (LPO) product accumulation, protein inactivation, and DNA damage, thus eliciting oxidative stress and cell apoptosis [8–13]. Despite several advantages, including high tumor selectivity, low side effects, and no dependence on equipment and external energy input, the anticancer efficacy of CDT is largely restricted by high expression of the intracellular antioxidant glutathione (GSH) (up to 2–10 mM) and the limited amount of H_2O_2 (commonly 100 μM) in tumor tissues [14–18]. To improve CDT potency, some novel tactics for promoting intracellular GSH consumption and H_2O_2 generation have been developed [14–19]. There are two common routes to accomplish GSH depletion, including conjugation of GSH with specific molecules to form GS-X adducts [20,21] and oxidation of GSH with metal ions (such as Fe^{3+} , Cu^{2+} , and Mn^{3+}) [16,22]. Moreover, in addition to frequently utilized glucose oxidase capable of catalyzing the conversion of glucose to gluconic acid and H_2O_2 [11,23], some chemotherapy (CT) drugs such as doxorubicin (DOX), cisplatin, and camptothecin have been demonstrated to enhance H_2O_2 concentration in tumor region [2,24,25]. Therefore, to boost the antitumor effect, substantial efforts have been devoted to combining CDT and CT in a single smart nanoplatform capable of depleting GSH and co-delivering CDT agents and CT drugs to tumor sites [25–28].

Some studies have reported that Fe^{2+} ions have significantly higher catalytic activity than Fe^{3+} ions in generating toxic $\bullet\text{OH}$ via the Fenton reaction [29,30]. Nevertheless, cellular ferritin stores iron in the form of Fe^{3+} as well as the inefficient intracellular reduction from Fe^{3+} to Fe^{2+} largely diminish the continuation of the Fenton reaction, thereby lowering the CDT-mediated anticancer effect [29,30]. Therefore, it is urgent to design a vehicle for the effective tumor-targeted delivery of Fe^{2+} to amplify the efficiency of CDT. A varied of metal-organic frameworks (MOFs) fabricated from the coordination of organic ligands and metal ions have emerged as suitable materials for applications such as catalysis, gas storage, drug delivery, gas vapor separation, lithium-ion batteries, water treatment, and carbon dioxide capture, as well as photo- and electrocatalysis [1–3,31–34]. Furthermore, MOFs are widely employed for luminescence sensing and chemical detection of nucleic acids, proteins, and small physiological molecules for cancer diagnosis [3]. Among them, the nano-scaled MOFs (nanoMOFs) have been extensively utilized as multifunctional carriers for metal ions, small-molecule drugs, and proteins due to their unique merits such as porosity, biodegradability, structural and functional diversity [5–8,35–40]. The zeolitic imidazolate framework-8 (ZIF-8), which is made up of zinc ions and 2-methyl imidazolate, has been broadly employed as a pH-responsive drug carrier in nanomedicine owing to the facile preparation, good biocompatibility, and rapid disintegration in the acidic tumor microenvironment [1,41–44]. Inspired by this, Wei and co-workers prepared a biodegradable Fe^{2+} -doped ZIF-8-based nanoconstruct capable of co-delivering DOX and indocyanine green (ICG), a

photothermal reagent [42]. By the integration of CDT, CT and photothermal therapy, the as-designed nanoconstruct exhibited a significant anticancer effect on HeLa cells (human cervical carcinoma). Also, Zhong et al. utilized a similar design to fabricate Fe^{2+} -doped ZIF-8 nanocomposites as DOX vehicles for a combination of DOX-mediated apoptosis and Fe^{2+} -activated ferroptosis [43]. On the other hand, Zhao's group developed polydopamine (PDA)-covered Cu^{2+} -doped ZIF-8 nanocomposites loaded with DOX (DOX@ Cu^{2+} /ZIF-8@PDA, DCZP) and demonstrated that the DCZP effectively inhibited tumor growth through GSH depletion and chemo/photothermal/chemodynamic combination therapy [1].

Despite significant progress of MOF-based delivery systems capable of combining CDT and CT, to the best of our knowledge, few studies on the Fe^{2+} -doped ZIF-8 nanoMOFs designed with dual GSH depletion and active tumor targeting homing were reported. Herein, it should be highlighted that the effective tumor-targeted delivery of the combined CDT and CT is required due to the short lifetime and diffusion distance of $\bullet\text{OH}$ in the tumor microenvironment as well as the systemic adverse effect of CT. Given the above considerations, in this work, a practical strategy was adopted to endow the Fe^{2+} -doped ZIF-8 nanoMOFs (FZ NMs) with dual GSH-consuming capability and specific tumor targeting for improved antitumor efficacy of the integrated CDT and CT. First, the FZ NMs were prepared and decorated with PDA layers that have been demonstrated to consume GSH via Michael addition [17,21,45]. Next, to equip the PDA-coated FZ NMs (PFZ NMs) with active targeting on CD44 that is overexpressed in many cancers [46,47], the CD44-targeting hyaluronic acid (HA) segments were partially modified with thiol groups and then covalently conjugated on the surfaces of PFZ NMs. Through the hydrophobic and π - π stacking interaction of DOX with PDA and its charge interactions with HA, the HPDFZ NMs with DOX payload (HPDFZ NMs) were attained (Scheme 1). The HPDFZ NMs exhibited robust colloidal stability in a serum-containing culture medium and promoted DOX and Fe^{2+} release in a weakly acidic and GSH-rich milieu. Moreover, the HPDFZ NMs effectively depleted GSH by PDA-mediated Michael addition combined with $\text{Fe}^{2+}/\text{Fe}^{3+}$ redox couple and accelerated conversion of H_2O_2 into $\bullet\text{OH}$ under weakly acidic conditions. After being internalized by CT26 cells via CD44-mediated endocytosis, the HPDFZ NMs prominently activated intracellular $\bullet\text{OH}$ generation and GSH depletion to cause mitochondria damage and LPO product accumulation, thereby potently killing cancer cells. The in vivo antitumor efficacy studies strongly demonstrated that the CT26 tumor-targeted CDT/CT delivery by HPDFZ NMs significantly retarded tumor progression without serious side effects. The work presented a promising strategy for designing versatile nanoMOFs with dual GSH depletion and combination therapy to realize tumor-specific treatment.

2. Materials and methods

2.1. Materials and cell lines

DOX (97 %) was acquired from Combi-Blocks (USA). Zinc nitrate hexahydrate (98 %), 2-methylimidazole (99 %), 2',7'-dichlorodihydrofluorescein diacetate (DCFH-DA, ≥ 97 %), 3-(4,5-Dimethylthiazol-2-yl)-2,5-diphenyltetrazolium bromide (MTT, ≥ 98 %), IR820 (80 %),

propidium (PI, 94 %), RPMI-1640 medium, D₂O (99.9 atom % D), Hoechst 33,342 (>98 %) were purchased from Sigma-Aldrich (USA). Ferrum (II) chloride (99.5 %), terephthalic acid (THA, 98 %), *N*-hydroxysuccinimide (NHS, 98 %), and dopamine hydrochloride (DA, 99 %) were attained from Alfa Aesar (USA). *N*-(3-Dimethylaminopropyl)-*N*'-ethylcarbodiimide hydrochloride (EDC-HCl, ≥ 95 %) was purchased from Fetal bovine serum (FBS) was purchased from Hyclone (USA). HA (Mw 30 k-50 k Da) was obtained from Glentham Life Science (UK). 5,5'-dithiobis (2-nitrobenzoic acid) (DTNB, ≥ 98 %) was purchased from Fluorochem (UK). JC-1 assay kit was purchased from MedChemExpress (USA). Calcein-AM was obtained from AAT Bioquest (USA). BODIPY™ 581/591 C11 was obtained from Thermo Fisher Scientific (USA). Anti-Ki67 antibodies (no. ab15580) and anti-glutathione peroxidase 4 (GPX4) antibodies (no. ab125066) were obtained Abcam. Deionized water was produced from Milli-Q Synthesis (18 MΩ, Millipore). All other chemicals were reagent grade and used as received. CT26 (murine cancer cell line), TRAPM-C1 (murine prostate cancer cell line) and WS1 (human skin fibroblast cells) cells were obtained from Food Industry Research and Development Institute (Hsinchu City, Taiwan).

2.2. Synthesis of FZ NMs and PFZ NMs

The FZ NMs were prepared using a method modified from the literature [42]. In brief, FeCl₂ (1.1 mg, 8.4 × 10⁻³ mmol) and Zn(NO₃)₂·6H₂O (22.5 mg, 75.6 × 10⁻³ mmol) were dissolved in deionized water (0.6 mL) and dropwise added into 1.0 mL deionized water containing 2-methylimidazole (250 mg). The solution was stirred at room temperature for 10 min, and the yellow FZ NMs were collected by centrifugation (10000 rpm, 10 min) and washed three times with deionized water. Finally, the FZ NMs were dispersed in deionized water for further use. For comparison, FZ NMs with different feeding ratios of Fe²⁺ ions to total moles of Zn²⁺ and Fe²⁺ ions (5 %, 20 %, and 30 %) were prepared in a similar manner. Next, PFZ NMs were prepared by the following

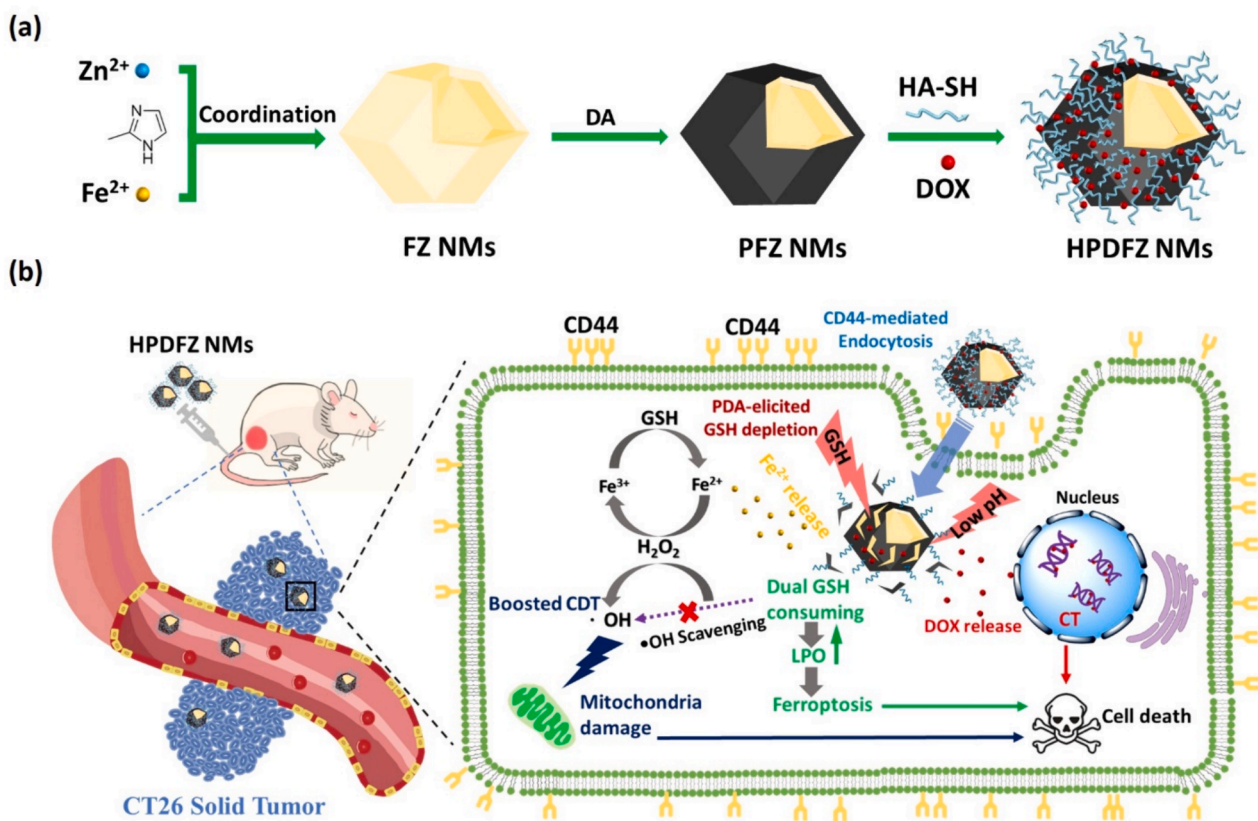
approach. First, the FZ NMs (4.0 mg) were dispersed in 2.0 mL of deionized water, and DA (4.0 mg) was dissolved in deionized water (2.0 mL) and stirred at 50 °C for 10 min. Afterward, the aqueous solution of FZ NMs was dropwise added into the DA solution, followed by the addition of 1 N NaOH (30 μL). The mixing solution was stirred at 50 °C for 5 h. PFZ NMs were then collected by centrifugation (12000 rpm, 5 min) and washed five times with deionized water to remove the unpolymers DA. Finally, the PFZ NMs were re-dispersed in deionized water for further use.

2.3. Synthesis and characterization of HA-SH

The HA-SH used in this work was synthesized by EDC/NHS-mediated amidation of cysteamine molecules and HA segments [48]. The detailed synthetic pathway of HA-SH is presented in Fig. 1a. First, HA (68.1 mg) and NHS (41.4 mg) were dissolved directly in deionized water (2.25 mL) under stirring at room temperature. Afterward, EDC (103.5 mg) in solid form was added to the mixing solution and reacted for 2 h to activate the carboxylic group of HA. Subsequently, cysteamine (60 mg) was dissolved in deionized water (0.45 mL) and added to the above solution. The pH of the mixing solution was adjusted to 5.0 by adding 1.0 N NaOH and stirred at room temperature for 24 h. Then, the solution was dialyzed (MWCO 12000–14000) against 0.1 M NaCl (pH 3.5) for 48 h and deionized water for 24 h, followed by lyophilization to collect the product. The chemical structures of HA and HA-SH were characterized by ¹H NMR (Agilent DD2 600 MHz NMR spectrometer) using D₂O as a solvent and FT-IR (FT-720 spectroscopy, HORIBA, Japan).

2.4. Synthesis of HPDFZ NMs

HPDFZ NMs were attained as follows. HA-SH in pH 8.0 phosphate buffer (100 μL, 9.0 mg/mL) was dropwise added into 800 μL aqueous solution containing PFZ NMs (1.0 mg), and the mixing solution was



Scheme 1. Schematic Illustration of (a) HPDFZ NMs fabrication and (b) antitumor performance of HPDFZ NMs.

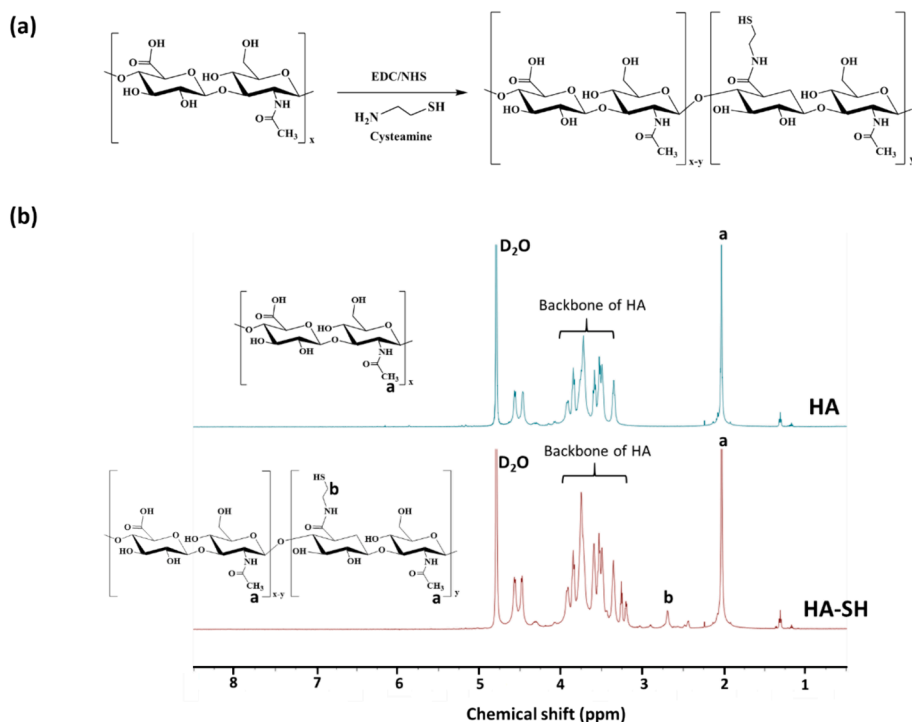


Fig. 1. (a) Synthetic route and chemical structure of HA-SH. (b) ¹H NMR spectra of HA and HA-SH in D₂O.

stirred at room temperature for 2 h. Afterward, DOX in DMSO (100 μ L, 2.0 mg/mL) was added to the above solution and stirred for 22 h. The solution containing HPDFZ NMs was dialyzed (MWCO 12000–14000) against pH 8.0 phosphate buffer to remove unloaded DOX and DMSO. For comparison, HPZ NMs, HPFZ NMs and HPDZ NMs were prepared in a similar way.

2.5. Characterization

Ultraviolet–visible (UV/vis) spectra were obtained using a UV/Vis spectrophotometer (V730, JASCO, Japan). A D8 Discover X-ray diffractometer (Bruker, Germany) with CuK α radiation (40 kV, $\lambda = 0.15$ nm) was utilized to attain the X-ray diffraction (XRD) patterns of various NMs. The mean hydrodynamic diameter (D_h) and size distribution (polydispersity index, PDI) of NMs dispersed in aqueous solutions were measured by a Brookhaven BI-200SM goniometer equipped with a BI-9000 AT digital correlator using a solid-state laser (35 mW, $\lambda = 637$ nm). The zeta potential of NMs in aqueous solutions was examined by a Litesizer 500 (Anton Paar, USA). The data shown herein represent an average of at least triplicate measurements. A transmission electron microscope (TEM) (JEM-1400 FLASH, JEOL, Japan) and a scanning electron microscope (SEM) (JEOL JSM-7800F Prime Schottky Field Emission SEM, Japan, an acceleration voltage of 3 kV) were employed to observe the morphologies of NMs [49,50]. X-ray photoelectron spectroscopy (XPS) analysis was conducted by a PHI 5000 VersaProbe III X-ray photoelectron spectrometer (ULVAC-PHI, Japan) with AlK α radiation ($h\nu = 1486.6$ eV) at 15 kV and 150 W. Thermogravimetric analysis (TGA) of FZ NMs and PFZ NMs was conducted with thermogravimetric analyzer EXSTAR TG/DTA 6200 (Seiko Instruments Inc) in an N₂ atmosphere by heating the sample to 900 $^{\circ}$ C at the rate of 10 $^{\circ}$ C/min [51].

2.6. Determination of Fe²⁺ and DOX content

To quantify the Fe²⁺ content of various NMs, a prescribed amount of the purified NMs was diluted 20 times with HNO₃ solution (1 %) and the mixture was then stirred for 24 h to completely dissociate the iron. The Fe²⁺ concentration was quantified by inductively coupled plasma-

atomic emission spectrometry (ICP-AES) with an Agilent 725 emission spectrometer. The Fe²⁺ loading content was estimated by the following equation:

$$\text{LC of Fe}^{2+} (\%) = (\text{weight of Fe}^{2+} \text{ loaded} / \text{total weight of Fe}^{2+}\text{-doped NMs}) \times 100 \%$$

The DOX loading content of different DOX-carrying NMs was determined as follows. Before dialysis for purification, the solution of DOX-containing NMs (100 μ L) was centrifuged (16000 rpm, 10 min), the supernatant was withdrawn, and the fluorescence intensity of DOX (ex: 480 nm, em: 500–700 nm) was measured by a fluorescence spectrophotometer (Hitachi F-2700). The calibration curve used for drug loading characterization was established by fluorescence intensity of DOX with various concentrations in DMSO/deionized water (1/9 (v/v)) solution. The loading content (LC) of DOX was calculated by the following formula:

$$\text{LC of DOX} (\%) = ((\text{weight of DOX in feed} - \text{weight of DOX in the supernatant}) / \text{total weight of DOX-carrying NMs}) \times 100 \%$$

2.7. In vitro DOX and Fe²⁺ release study

For DOX liberation measurement, the HPDFZ NM solution (1.0 mL) was dialyzed (Cellu Sep MWCO 12000 ~ 14000) against phosphate buffer saline (PBS) of pH 7.4, acetate buffer of pH 5.0 and 4.0, and pH 5.0 acetate buffer containing 10 mM GSH (ionic strength 0.15 M, 20 mL), respectively, at 37 $^{\circ}$ C. At the prescribed time intervals, 1.0 mL of dialysate was taken for analysis and replaced with an equivalent volume of fresh buffer. The amount of DOX released was measured by fluorescence measurement.

For Fe²⁺ release study, the HPDFZ NM solution (1.0 mL) was dialyzed (Cellu Sep MWCO 12000–14000) against pH 7.4 PBS and pH 5.0 acetate buffer containing 10 mM GSH or not (ionic strength 0.15 M, 20 mL), respectively, at 37 $^{\circ}$ C. At the prescribed time intervals, 1.0 mL of dialysate was taken for analysis and replaced with an equivalent volume of fresh buffer. The amount of Fe²⁺ released was analyzed by ICP-AES.

2.8. GSH depletion capability assessment

The GSH-depleting capability of various NMs was evaluated by DTNB assay. Briefly, 800 μL aqueous solution containing Z NMs (37.5 $\mu\text{g}/\text{mL}$), FZ NMs (37.5 $\mu\text{g}/\text{mL}$), PFZ NMs (50 $\mu\text{g}/\text{mL}$) or HPFZ NMs (50 $\mu\text{g}/\text{mL}$) were added to 100 μL of GSH solution (0.68 mM) and incubated at 37 °C for 1, 4 and 8 h. Next, the resulting solution was centrifugated to collect the supernatant. Then, DTNB (80 μL , 0.61 mM) was added to the supernatant, and the absorbance of the mixture at 412 nm was measured. The calibration curve employed for GSH concentration analysis was established by absorbance of DTNB treated with GSH of various concentrations. The GSH content of the mixture was calculated by the following formula:

Residual GSH content (%) = (GSH concentration of the mixture attained at different time points/GSH concentration in feed).

2.9. Chemodynamic effect

The catalytic activity ($\bullet\text{OH}$ generation) of different NMs at pH 7.4 and 5.0 was evaluated by determining the fluorescence intensity of 2-hydroxyterephthalic acid generated from the reaction of THA with $\bullet\text{OH}$. Briefly, Z NMs (37.5 $\mu\text{g}/\text{mL}$), FZ NMs (37.5 $\mu\text{g}/\text{mL}$), PFZ NMs (50 $\mu\text{g}/\text{mL}$), or HPDFZ NMs (50 $\mu\text{g}/\text{mL}$) were dispersed in pH 7.4 phosphate buffer and pH 5.0 acetate buffer containing 8 mM H_2O_2 and 50 μM THA. The mixing solutions were incubated in the dark at 37 °C for different time intervals. The fluorescence intensity of 2-hydroxyterephthalic acid at 420 nm was determined by a fluorescence spectrophotometer (Hitachi F-2700). Moreover, in the presence of GSH (2 mM), the $\bullet\text{OH}$ generation of FZ NMs and PFZ NMs (Fe^{2+} concentration = 0.625 $\mu\text{g}/\text{mL}$) in pH 5.0 acetate buffer containing H_2O_2 (8 mM) and 50 μM THA was explored in a similar manner. Furthermore, the HPDFZ NMs of different concentrations were dispersed in pH 5.0 acetate buffer containing H_2O_2 (8 mM) and MB (10 $\mu\text{g}/\text{mL}$). The mixing solutions were incubated at 37 °C for 3 h and then centrifugated (16000 rpm, 10 min) to collect supernatant. The UV/vis spectrum of MB in the supernatant was attained with a UV/Vis spectrophotometer.

2.10. In vitro cellular uptake

The CD44-overexpressed CT26 cells (2×10^5 cells/well) seeded in 6-well plates were incubated with free DOX molecules, HPDFZ NMs with or without free HA (DOX concentration = 10 μM , HA concentration = 200 $\mu\text{g}/\text{mL}$), respectively, at 37 °C for 1 and 4 h. After being detached with trypsin-EDTA solution, the DOX fluorescence signals of the treated CT26 cells suspended in PBS (1.0 mL) were analyzed by the FACSCalibur flow cytometer (BD Bioscience). On the other hand, CT26 cells (2×10^5 cells/well) seeded onto 22 mm round glass coverslips in 6-well plates were incubated with free DOX molecules, HPDFZ NMs with or without free HA (DOX concentration = 10 μM , HA concentration = 200 $\mu\text{g}/\text{mL}$), respectively, for 1 and 4 h at 37 °C. After being rinsed two times with Hanks' balanced salt solution (HBSS) and immobilized with 4 % formaldehyde, the cell nuclei were stained with Hoechst 33342. The cellular images were obtained by confocal laser scanning microscope (CLSM) (Olympus, FluoView FV3000, Japan) at the excitation wavelengths of 405 and 480 nm for Hoechst and DOX, respectively.

2.11. Intracellular GSH depletion and $\bullet\text{OH}$ generation

To assess intracellular GSH depletion, CT26 cells (3.0×10^5 /well) seeded in a 6-well plate were incubated with Z NMs (62.5 $\mu\text{g}/\text{mL}$), FZ NMs (62.5 $\mu\text{g}/\text{mL}$) and HPDFZ NMs (62.5 $\mu\text{g}/\text{mL}$), respectively, at 37 °C for 6 h. After being washed twice with PBS, the treated cells were detached with trypsin-EDTA and then centrifugated (1500 rpm, 5 min). The collected cell pellets were re-dispersed in 0.3 mL RIPA buffer, followed by freezing and thawing for cell lysis. The cell-containing solution was centrifuged (12000 rpm, 10 min), and the supernatant was

withdrawn for analysis. The intracellular GSH level of each group was examined by DTNB-thiol assay using a microplate reader at a wavelength of 405 nm.

On the other hand, to explore the intracellular $\bullet\text{OH}$ generation, CT26 cells (3×10^5 cells/well) seeded onto 22 mm round glass coverslips in 6-well plates were incubated with free DOX molecules (10 μM) and various NMs (NM concentration = 62.5 $\mu\text{g}/\text{mL}$), respectively, at 37 °C for 6 h. After discarding the culture medium, the cells were treated with DCFH-DA (10 μM) for 30 min and rinsed twice with HBSS, followed by immobilization with 4 % formaldehyde. The cellular images were attained using fluorescence microscopy (ZEISS Axio Imager M2) at excitation wavelengths of 485 nm for DCF.

2.12. Mitochondrial membrane potential analysis

CT26 cells (3×10^5 /well) seeded in a 6-well plate containing 22 mm round glass coverslips were incubated with free DOX molecules (10 μM) and various NMs (NM concentration = 62.5 $\mu\text{g}/\text{mL}$), respectively, at 37 °C for 24 h. After removing the culture medium, the cells were exposed to JC-1 (2 μM) for 30 min and then rinsed twice with HBSS. Subsequently, the cells were fixed with 4 % formaldehyde and observed using fluorescence microscopy (ZEISS Axio Imager M2) at excitation wavelengths of 485 and 535 nm for JC-1 monomer and JC-1 aggregate, respectively.

2.13. Intracellular LPO detection

CT26 cells (3×10^5 /well) seeded onto 22 mm round glass coverslips in a 6-well plate were incubated with free DOX molecules (10 μM) and various NMs (NM concentration = 62.5 $\mu\text{g}/\text{mL}$), respectively, at 37 °C for 24 h. After removal of the culture medium, the cells were incubated with BODIPYTM 581/591 C11 (5 μM) for 30 min and washed twice with HBSS, followed by immobilization with 4 % formaldehyde. Finally, the intracellular lipoperoxidation was observed by fluorescence microscopy (ZEISS Axio Imager M2).

2.14. In vitro anticancer efficacy of combined CDT and CT

To evaluate the cytotoxicity of different NMs on cancer cells, the MTT assay was used [52]. CT26 cells (1.0×10^4 cells/well) seeded in a 96-well plate were incubated at 37 °C for 24 h in RPMI-1640 containing 10 % FBS and 1 % penicillin. The medium was then replaced with 100 μL of fresh medium containing free DOX molecules, HPZ NMs, HPFZ NMs, HPDZ NMs, or HPDFZ NMs of different concentrations and incubated for an additional 24 h. After being washed twice with PBS, MTT (0.25 mg/mL, 100 μL) was added into each well and further incubated at 37 °C for 3 h. Then, the supernatant was removed and the precipitates were dissolved in DMSO (120 μL), and the absorbance per well at 570 nm was measured by a BioTek 800TS microplate reader. Besides, the CDT/CT-mediated anticancer effect of HPDFZ NMs on TRAMP-C1 cells was assessed in a similar manner.

On the other hand, to explore the anticancer effect of different NMs on CT26 cells, the fluorescence staining of live/dead cells was conducted [53]. CT26 cells (2×10^5 cells/well) seeded in a 12-well plate were incubated with free DOX molecules, HPZ NMs, HPFZ NMs, HPDZ NMs or HPDFZ NMs (DOX concentration = 10 μM , NM concentration = 62.5 $\mu\text{g}/\text{mL}$) at 37 °C for 24 h. Subsequently, cells were washed twice with HBSS, followed by staining with Calcein AM (2 μM) and PI (4.5 μM). The fluorescence imaging was observed by a NIB-100F inverted fluorescent biological microscope.

2.15. IR820 labeling of HPFZ NMs

HA-SH in pH 8.0 phosphate buffer (100 μL , 9.0 mg/mL) was dropwise added into 800 μL aqueous solution containing PFZ NMs (1.0 mg) and the mixing solution was stirred at room temperature for 2 h.

Afterward, IR820 in DMSO (100 μ L, 2.0 mg/mL) was added into the above solution and stirred for 22 h. The solution containing IR820@HPFZ NMs was dialyzed (MWCO 12000–14000) against pH 8.0 phosphate buffer to remove unloaded IR820 and DMSO. The mean hydrodynamic diameter of IR820@HPFZ NMs was determined by a Brookhaven BI-200SM goniometer equipped with a BI-9000 AT digital correlator using a solid-state laser (35 mW, $\lambda = 637$ nm). The IR820 loading content of was determined as follows. Before dialysis for purification, the solution of IR820@HPFZ NMs (100 μ L) were centrifuged (16000 rpm, 10 min), and the supernatant was withdrawn and the absorbance of IR820 at 700 nm was measured by a UV/Vis spectrophotometer (V730, JASCO, Japan). The calibration curve used for IR820 loading characterization was attained by absorbance of IR820 with various concentrations in DMSO/deionized water (1/9 (v/v)) solution. The IR820 loading content was calculated by the following formula: Loading content of IR820 (%) = ((weight of IR820 in feed – weight of IR820 in the supernatant)/total weight of IR820@HPFZ NMs) \times 100 %.

2.16. Animals and tumor model

Female BALB/c mice (5 ~ 6 weeks old) purchased from the National Laboratory Animal Center (Taiwan) were cared according to the Guidance Suggestions for the Care and Use of Laboratory Animals, approved by the Administrative Committee on Animal Research in the Chung Shan Medical University (Taiwan) (IACUC Approval No: 2719). 5×10^6 CT26 cells were subcutaneously injected into the right thigh of mice, and the tumor model was attained 10 days post-inoculation. Tumor volume (V) was calculated as follows: $V = L \times W^2 / 2$, where W is the tumor measurement at the widest point and L the tumor dimension at the longest point.

2.17. In vivo imaging and biodistribution

To observe the in vivo biodistribution of HA/PDA-modified NMs by an IVIS imaging system, a hydrophobic near-infrared (NIR) dye, IR820, was encapsulated into these NMs. The IR820@HPFZ NMs were prepared as described above. When the tumor volume of all mice reached 100 ~ 150 mm³, the CT26 tumor-bearing mice were intravenously injected with PBS, free IR820 molecules, and IR820@HPFZ NMs (dosage of 1.7 mg/kg IR820), respectively. The in vivo biodistribution of free IR820 molecules and IR820@HPFZ NMs was evaluated by observing fluorescence signals of IR820 (Ex. 710 nm and Em. 760 nm) at 2, 4, 6, and 24 h post-injection with an IVIS imaging system (IVIS Lumina II, Caliper, LifeSciences, MA, USA). The treated mice were sacrificed by CO₂ euthanasia at 24 h post-injection, and the major organs and tumors were gathered for imaging by IVIS.

2.18. In vivo tumor growth inhibition

When the tumor volume of mice reached 100 ~ 150 mm³, mice were randomly divided into 5 groups (n = 3 per group): (i) PBS; (ii) HPFZ NMs; (iii) HPDZ NMs; (iv) HPDFZ NMs; (v) free DOX molecules. Mice in different groups were intravenously injected with the corresponding reagents at a DOX dosage of 1.3 mg/kg and a Fe²⁺ dosage of 0.16 mg/kg. The first four groups were treated with a total of two doses on days 0 and 2. The final group was treated with a total of three doses on days 0, 2, and 4. The tumor volume and body weight of CT26 tumor-bearing mice in different groups were measured every two days until 18 days post-treatment. After all mice were euthanized, the tumors and main organs, including heart, liver, spleen, lung, and kidney, were gathered. Then, the collected tumors were weighed. The harvested tumors and organs were fixed with 4 % paraformaldehyde and then processed routinely in paraffin. After being stained with H&E, anti-Ki67 antibodies, and anti-GPX4 antibodies, respectively, tumor sections were observed by digital microscope.

2.19. Statistical analysis

Data are reported as mean \pm SD. The differences among groups were determined using one-way or two-way ANOVA analysis; ns > 0.05, *p < 0.05, **p < 0.01, ***p < 0.001.

3. Results and discussion

3.1. Synthesis and characterization of ZIF-8 NMs (Z NMs) and FZ NMs

Through the coordination of 2-methylimidazole with zinc nitrate, Z NMs were synthesized in a previously reported manner [42]. To boost CDT by generating enough toxic \bullet OH upon Fenton reaction, the Fe²⁺ ions (10 % with respect to total moles of Zn²⁺ and Fe²⁺ ions) were doped into Z NMs to obtain FZ NMs. As shown in Fig. 2a, the absorption of FZ NMs in 300 ~ 400 nm was appreciably enhanced relative to Z NMs, being ascribed to the presence of Fe²⁺ ions capable of causing a shift in the band gap of FZ NMs [54]. Also, different from the Z NM solution with slight grey-blue, the FZ NM solution displayed brightly yellow. These findings indicate the successful incorporation of Fe²⁺ ions into Z NMs. Furthermore, the XRD patterns of Z NMs and FZ NMs are comparable to the simulated one of ZIF-8 (Fig. 2b), demonstrating that the doped Fe²⁺ has no obvious effect on the crystal structure of Z NMs. The SEM images further showed that the Z NMs and FZ NMs exhibited 3-D cubic morphologies with truncated edges (Fig. S1). As presented in the TEM images (Fig. 2c), the size (ca 99.2 nm) of FZ NMs was appreciably larger than that (83.7 nm) of Z NMs. The mean hydrodynamic diameter of FZ NMs dispersed in pH 7.4 0.01 M phosphate buffer was determined to be ca 164.2 nm was also larger compared to that (127.4 nm) of Z NMs under the same condition (Fig. 2d). Notably, as the feeding ratio of Fe²⁺ ions to total moles of Zn²⁺ and Fe²⁺ ions was adjusted from 10 to 30 %, in addition to the increased PDI, the particle size of FZ NMs in pH 7.4 phosphate buffer was remarkably enlarged from ca 164.2 to 360.0 nm (Fig. 2e). Such an increased size of Z NMs after being doped with Fe²⁺ ions could be attributed to the larger radii of Fe²⁺ (0.76 Å) than Zn²⁺ (0.74 Å) [55]. With more Zn²⁺ sites being replaced by Fe²⁺ ions with a large ionic radius, the size of FZ NMs was gradually enlarged. A similar result was also reported elsewhere [42]. Based on the above results, the FZ NMs with a Fe²⁺ feeding ratio of 10 % were utilized in the following work due to their small particle size and narrow size distribution. On the other hand, the chemical structure of the resulting FZ NMs was characterized with XPS. The peaks at 710.9 eV and 724.3 eV assigned to Fe (2p_{3/2}) and Fe(2p_{1/2}) of Fe²⁺, respectively, and the characteristic satellite peak at around 718.1 eV also resulted from Fe²⁺ were observed in Fig. 2f, confirming the presence of Fe²⁺ ions in the FZ NMs [42,56].

3.2. Synthesis and characterization of PFZ NMs and HPDFZ NMs

Several studies report that a high level of GSH in cancer cells can largely scavenge intracellular \bullet OH to reduce oxidative injury, thus diminishing the anticancer potency of CDT [14–18]. The biomimetic PDA has been demonstrated to consume intracellular GSH upon Michael addition between the quinone moieties of PDA and the thiol group of GSH [17,21]. Consequently, the surface of FZ NMs was coated with a PDA layer by in situ self-polymerization of DA molecules to boost their CDT-mediated antitumor efficacy by reducing intracellular GSH levels. As shown in Fig. 2a, compared to FZ NMs, the attained PFZ NMs in aqueous solution exhibited enhanced absorption from 300 to 800 nm. Furthermore, the PFZ NM solution displayed a black color, distinct from the yellow color of the FZ NM solution. These results indicate the successful incorporation of PDA with FZ NMs. Based on the TGA profiles (Fig. S2), the PFZ NMs were composed of ca 78.5 wt% FZ NMs and 21.5 wt% PDA. Notably, the XRD profile of PFZ NMs was similar to that of FZ NMs and Z NMs (Fig. 2b), verifying that the crystal structure of FZ NMs was unaffected by the PDA surface coating. As shown in the TEM images (Fig. 2c and fig. S3), the PFZ NMs possessed a cubic-like shape and a size

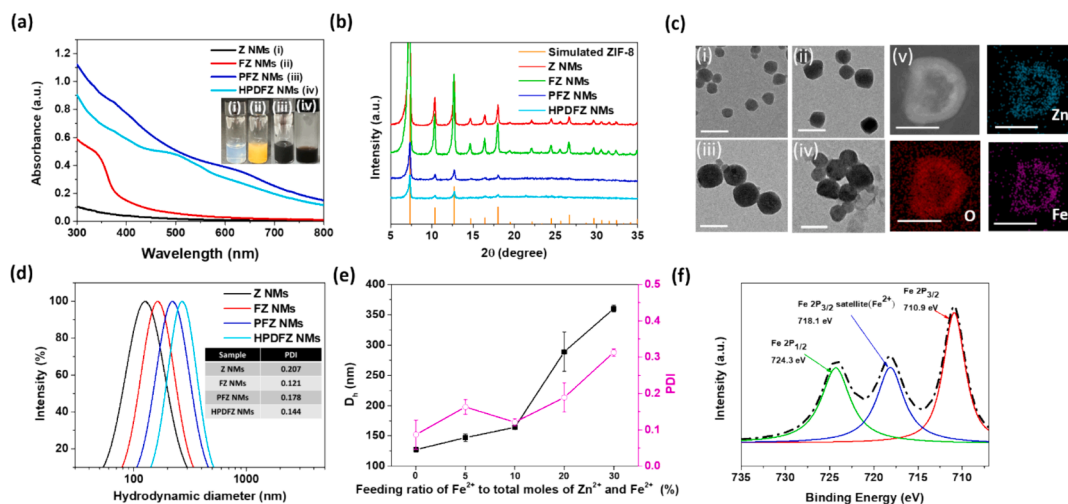


Fig. 2. (a) UV/Vis spectra of Z NMs, FZ NMs, PFZ NMs, and HPDFZ NMs in deionized water. (b) XRD patterns of Z NMs, FZ NMs, PFZ NMs, HPDFZ NMs, and simulated ZIF-8. (c) TEM images of (i) Z NMs, (ii) FZ NMs, (iii) PFZ NMs and (iv) HPDFZ NMs. Scale bars are 200 nm. X-ray EDS elemental maps of (v) HPDFZ NMs. Scale bars are 200 nm. (d) Particle size distribution profiles and PDI data of Z NMs, FZ NMs, PFZ NMs, and HPDFZ NMs in pH 7.4 0.01 M phosphate buffer. (e) Mean hydrodynamic diameter and PDI of FZ NMs with different feeding ratios of Fe^{2+} to total moles of Zn^{2+} and Fe^{2+} . (f) High-resolution Fe 2p XPS spectra of FZ NMs.

of around 153 nm, slightly larger than FZ NMs. Considering the variance in particle size between FZ NMs and PFZ NMs, the thickness of the PDA layer was estimated to be approximately 27 nm. Also, the enlarged particle size of FZ NMs after being coated with PDA layer was observed in Fig. 2d. The covering of PDA layer on the surface of FZ NMs resulted in negative zeta potential of -18.9 mV for PFZ NMs due to the presence of negatively-charged phenolic hydroxyl groups in the PDA layer (Fig. 3a). Despite the successful decoration of PDA on the surfaces of FZ NMs, the attained PFZ NMs dispersed in pH 7.4 0.15 M PBS mimicking physiological salt condition tended to aggregate into precipitates (Fig. S4), being not beneficial for tumor-targeted drug delivery.

In this work, the hydrophilic HA-SH segments used as crucial surface coating materials were synthesized and characterized by ^1H NMR (Fig. 1b). Based on the signal integral ratio of the methylene protons (δ 2.7 ppm) of cysteamine and the acetyl methyl protons (δ 2.0 ppm) from

HA, the degree of substitution of HA with cysteamine defined here as the number of thiol group per 100 β -D-glucuronic acid (GlcUA)- β -D-glucosamine (GlcNAc) units was attained to be ca 11.2. To improve the colloidal stability of PFZ NMs and endow their capability of actively targeting CD44-overexpressed cancer cells, the HA-SH segments (90 % with respect to the weight of PFZ NMs in feed) were covalently conjugated on the surfaces of PFZ NMs upon the Michael addition between thiol groups of HA-SH and quinone residues of PDA (Scheme 1a). Notably, unlike the visible precipitates of PFZ NMs in pH 7.4 0.15 M PBS, the stable suspension of HPDFZ NMs in the same environment was achieved (Fig. S4). Next, through the hydrophobic and π - π stacking interaction of DOX with PDA and its charge interactions with HA, DOX molecules were encapsulated within HA/PDA-constituted layers of HPDFZ NMs. As presented in Table 1 and Fig. 2d, when the PFZ NMs were adorned with HA-SH segments and either loaded with DOX or not,

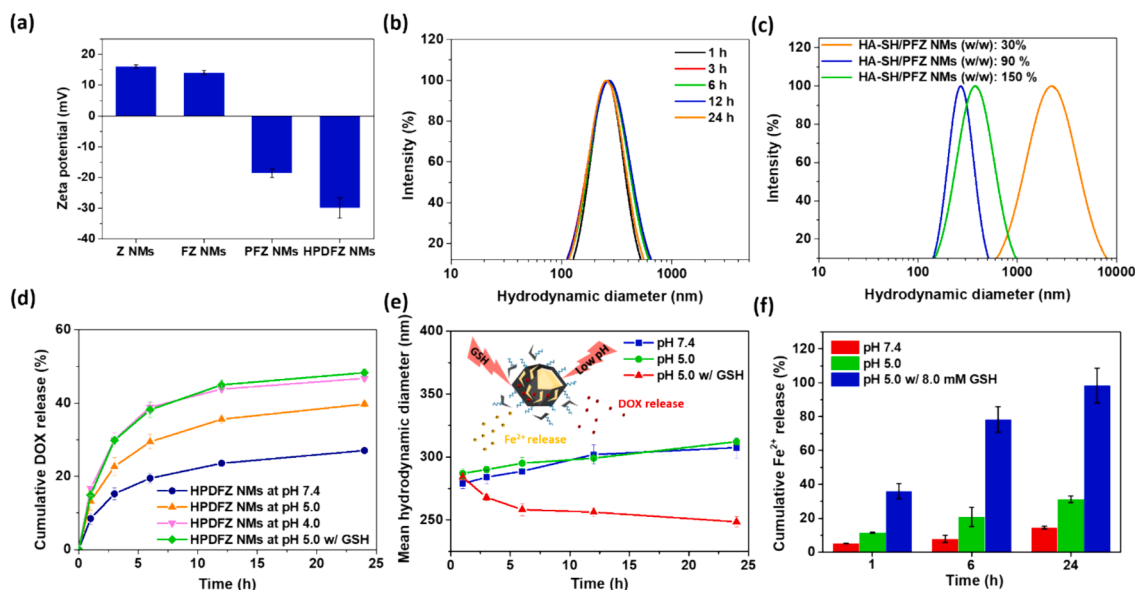


Fig. 3. (a) Zeta potential of Z NMs, FZ NMs, PFZ NMs, and HPDFZ NMs in pH 7.4 aqueous solution. (b) Particle size distribution profiles of HPDFZ NMs dispersed in 10 % FBS-containing RPMI 1640 culture medium at different time intervals. (c) Particle size distribution profiles of HPDFZ NMs with various feeding weight ratios of HA-SH and PFZ NMs. (d) Cumulative DOX release profiles of HPDFZ NMs under different conditions. (e) Time-evolved mean hydrodynamic diameter of HPDFZ NMs under different conditions. (f) Cumulative Fe^{2+} release profiles of HPDFZ NMs under different conditions.

Table 1
Particle size and Fe²⁺/DOX loading capability of NMs.

Sample	D _h (nm)	PDI	Fe ²⁺ loading content (wt %)	DOX loading content (wt %)
HPZ NMs	258.0 ± 6.8	0.135	–	–
HPFZ NMs	260.8 ± 14.4	0.128	1.0 ± 0.25	–
HPDZ NMs	272.6 ± 7.9	0.165	–	8.8 ± 0.04
HPDFZ NMs	281.2 ± 6.8	0.144	1.1 ± 0.17	8.9 ± 0.01

their average hydrodynamic diameter increased gradually from 227.5 to 260.8 nm (for HPFZ NMs) and 281.2 nm (for HPDFZ NMs), respectively. Moreover, the somewhat larger particle size of HPDFZ NMs as compared to that of PFZ NMs was observed in the TEM images (Fig. 2c). Note that the feature absorption of DOX at 480 nm was attained in the UV/Vis spectrum of HPDFZ NMs (Fig. 2a). Moreover, the surface decoration of HA led to a more negative zeta potential of −29.9 mV for HPDFZ NMs because of the massive negatively-charged carboxylic groups of HA (Fig. 3a). The findings suggest that DOX molecules and negatively-charged HA segments could be effectively incorporated into PFZ NMs. Notably, the HPDFZ NMs maintained nearly unvaried particle size in 10 % FBS-containing RPMI medium for 24 h (Fig. 3b). However, as the HA-SH feeding weight ratio was reduced from 90 to 30 %, the attained HPDFZ NMs were apt to aggregate into quite large particles (over 2000 nm) in pH 7.4 0.15 M PBS (Fig. 3c). Moreover, the increase of the HA-SH feeding weight ratio from 90 to 150 % led to an enlargement in the particle size of HPDFZ NMs. This could be attributed to the occurrence of excess HA-mediated inter-particle cross-linking. Based on these results, the appropriate amount of hydrophilic HA segments adorned on the surfaces of HPDFZ NMs is crucial in enhancing their colloidal stability. As a result, the HPDFZ NMs created with a HA-SH feeding weight ratio of 90 % were used in subsequent *in vitro* and *in vivo* studies because of their exceptional colloidal stability. On the other hand, according to the XRD pattern and TEM images (Fig. 2b and c), the crystal structure and cubic-like shape of the HPDFZ NMs closely resembled those of Z NMs and PFZ NMs. The elemental mapping images further confirm that the Fe²⁺ and Zn²⁺ ions coexist in the HPDFZ NMs (Fig. 2c). Interestingly, more Fe²⁺ and Zn²⁺ signals were observed in the PDA/HA-constituted layer. This may be ascribed to that some Fe²⁺ and Zn²⁺ ions from HPDFZ NMs tend to migrate into PDA-rich layers through their coordination interaction with the catechol groups of PDA [17,57]. The DOX and Fe²⁺ loading content of HPDFZ NMs were determined to be ca 8.9 wt% and 1.1 wt%, respectively (Table 1). Moreover, the HPFZ NMs and HPDZ NMs showed Fe²⁺ or DOX loading capacity comparable to HPDFZ NMs.

3.3. *In vitro* DOX and Fe²⁺ release of HPDFZ NMs

Considering the innate pH difference between the blood/normal tissues (pH 7.4) and intracellular acidic endosomes and lysosomes (pH 6.0–4.5) as well as the GSH-rich nature of cancer cells (2–10 mM), the *in vitro* DOX and Fe²⁺ dissolution of HPDFZ NMs were studied in aqueous solutions of different pH containing GSH or not. As shown in Fig. 3d, in the lack of GSH, when the solution pH was adjusted from 7.4 to 4.0, the cumulative DOX release over 24 h was remarkably increased from 27.0 to 46.7 %. Such an acidity-activated DOX liberation of HPDFZ NMs could be attributed to the following reasons. First, the hydrophobic and π - π interaction of DOX molecules with PDA layers of HPDFZ NMs in an acidic milieu were lowered due to acidity-elicited protonation of DOX. Moreover, the ionic pairings of DOX molecules with HA segments were considerably disintegrated because of the reduced dissociation degree of HA segments under acidic conditions. Interestingly, in the presence of 8 mM GSH, the cumulative DOX release of HPDFZ NMs at pH 5.0 for 24 h was further increased. Also, the HPDFZ NMs dispersed in a GSH-

containing aqueous solution of pH 5.0 exhibited gradually reduced particle size over time (Fig. 3e). By contrast, in the lack of GSH, the HPDFZ NMs showed virtually unchanged particle size at pH 7.4 and 5.0, respectively. Based on the above findings, it was assumed that the reductive GSH may change or even destroy the polymerization state of PDA, thus disrupting the HA/PDA-constituted layer of HPDFZ NMs to accelerate DOX outflow. Such a GSH-triggered drug release from PDA-containing nanovehicles was also reported elsewhere [58,59]. On the other hand, with solution pH being changed from 7.4 to 5.0, the cumulative Fe²⁺ liberation of HPDFZ NMs was somewhat increased from 14.5 to 31.2 % during 24 h (Fig. 3f), being ascribed to that the coordination bonds between the imidazole groups and Fe²⁺/Zn²⁺ ions of NMs became unstable due to the acidity-elicited protonation of imidazole groups. More importantly, virtually complete Fe²⁺ release from HPDFZ NMs was achieved at pH 5.0 in the existence of 8.0 mM GSH, indicating that the GSH-induced disintegration of the PDA layer could remarkably speed the outflow of Fe²⁺ ions. As shown in Fig. S5a, for HPDFZ NMs pretreated with GSH-containing solution at pH 5.0 for 24 h, some HPDFZ NMs exhibited appreciably reduced particle size, and visible Fe-based clusters were observed. By contrast, without GSH treatment, the HPDFZ NMs retained intact structure at pH 5.0 (Fig. S5b), similar to counterparts at pH 7.4. This further verifies the rapid release of Fe²⁺ from HPDFZ NMs in GSH-rich aqueous solution of pH 5.0. Interestingly, compared to the nearly complete release of Fe²⁺ from HPDFZ NMs at pH 5.0 in the presence of GSH during 24 h, only 48.3 % of DOX was liberated from HPDFZ NMs. This could be attributed to the following reasons. Firstly, the aforementioned multiple interactions of DOX with PDA and HA restricted the outflow of DOX from HPDFZ NMs. Moreover, DOX molecules are more hydrophobic than Fe²⁺ ions, thus tending to aggregate, reducing the diffusion rate. In conclusion, the HPDFZ NMs developed herein preserve the intact colloidal structure while allowing DOX and Fe²⁺ loading and retention in an effective manner at pH 7.4. Also, the HPDFZ NMs exhibit prominent payload liberation under weakly acidic and GSH-rich conditions, thus demonstrating great promise in intracellular cargo delivery.

3.4. GSH depletion and •OH generation

The GSH depletion capability of various NMs fabricated in this study was assessed by DTNB as the probe with a maximum absorbance at 408 nm [60]. The absorbance of DTNB in the Z NMs + GSH group was identical to that of DTNB in the GSH alone group as the control (Fig. 4a), indicating the lack of GSH depletion ability for Z NMs. Compared to the Z NMs + GSH group, the FZ NMs + GSH group somewhat decreased DTNB absorbance, being ascribed to that the minor amount of Fe³⁺ ions within FZ NMs could consume GSH via GSH-mediated Fe³⁺ reduction. Notably, the absorbance of DTNB in PFZ NMs + GSH group was appreciably declined in comparison with that of DTNB in FZ NMs + GSH group, proving that the incorporation of PDA layer can further deplete GSH via Michael addition between the quinone moieties of PDA and thiol group of GSH. Based on the similar absorbance of DTNB in HPFZ NMs + GSH group and PFZ NMs + GSH group, respectively, it was verified that the extra HA coating on the surfaces of PFZ NMs could not significantly affect their GSH-depleting ability. Furthermore, as presented in Fig. 4b, the HPFZ NMs and PFZ NMs efficiently consumed GSH over time compared to FZ NMs and Z NMs.

Next, the •OH-generating activity of HPDFZ NMs upon the Fenton reaction was explored by using THA as an indicator, which showed enhanced fluorescence at 420 nm after being reacted with •OH. In the presence of H₂O₂, the fluorescence intensity of THA in pH 5.0 aqueous solutions containing Z NMs or FZ NMs was remarkably higher than that of THA alone as the control (Fig. 4c). Moreover, compared to Z NM group, the FZ NM group showed the appreciably increased THA fluorescence over time (Fig. 4d). Based on these results, the FZ NMs were demonstrated to effectively promote conversion of H₂O₂ into •OH as compared to Z NMs due to Fenton catalytic activity of Fe²⁺ superior to

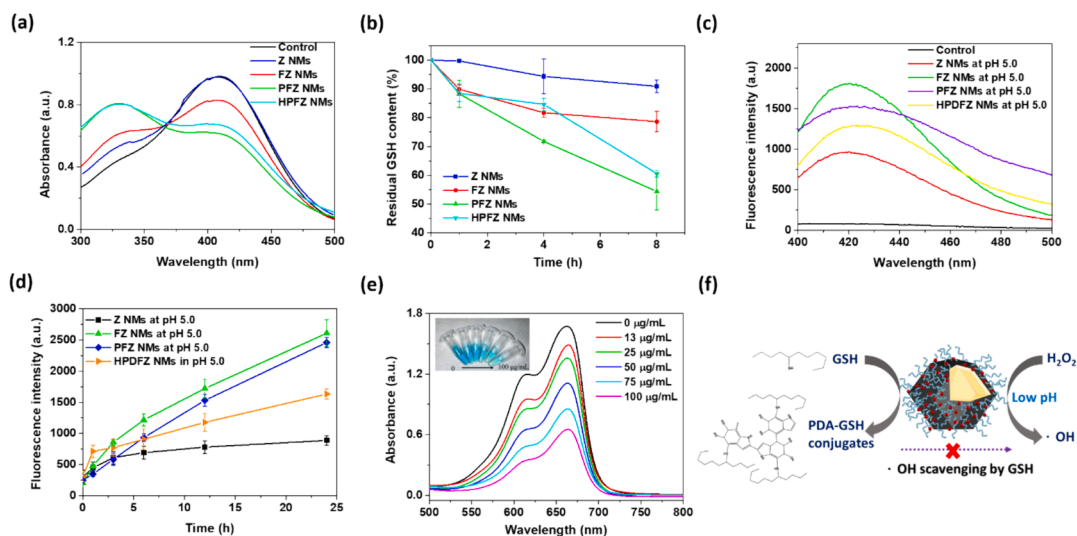


Fig. 4. (a) UV/Vis spectra of DTNB incubated with Z NMs, FZ NMs, PFZ NMs, and HPFZ NMs in the presence of GSH, respectively, for 8 h. (b) Residual content of GSH treated with Z NMs, FZ NMs, PFZ NMs, and HPDFZ NMs, respectively, for different time intervals. (c) Fluorescence spectra of THA incubated with Z NMs, FZ NMs, PFZ NMs, and HPDFZ NMs, respectively, in the presence of H_2O_2 at pH 5.0 for 12 h. (d) Fluorescence intensity of THA incubated with Z NMs, FZ NMs, PFZ NMs, and HPDFZ NMs, respectively, in the presence of H_2O_2 at pH 5.0 for different time intervals. (e) UV/Vis spectra of MB incubated with HPDFZ NMs of different concentrations in the presence of H_2O_2 at pH 5.0 for 3 h. (f) Schematic illustration of GSH depletion and $\bullet\text{OH}$ production of HPDFZ NMs.

Zn^{2+} . Notably, when the PDA and HA layer were sequentially coated on the surfaces of FZ NMs, the resulting PFZ NMs and HPDFZ NMs exhibited somewhat lowered Fenton catalytic activity as reflected in the decreased THA fluorescence intensity (Fig. 4c and d). This was probably attributed to that the spatial barrier of PDA and HA layers partly hindered Fe^{2+} release and H_2O_2 inflow, thus retarding $\bullet\text{OH}$ production. Despite this, the fluorescence intensity of THA in H_2O_2 -containing HPDFZ NM solution at pH 5.0 was gradually increased with the prolonged reaction time (Fig. 4d), signifying that the HPDFZ NMs sustainably generated $\bullet\text{OH}$ upon the Fenton reaction between H_2O_2 and the released Fe^{2+} ions. On the other hand, in the presence of H_2O_2 , with the solution pH being adjusted from 5.0 to 7.4, the increase in fluorescence intensity of THA in aqueous solutions of different NMs over 24 h was significantly restricted (Fig. S6), suggesting the limited generation of $\bullet\text{OH}$. As expected, the highly efficient Fenton reaction favors occur in acidic conditions [39,61,62]. The $\bullet\text{OH}$ -generating capability of HPDFZ NMs at pH 5.0 was also evaluated by using MB assay. As revealed in Fig. 4e, in the presence of H_2O_2 at pH 5.0, the absorbance of MB at 660 nm was remarkably decreased with the increased concentration of HPDFZ NMs from 0 to 100 $\mu\text{g}/\text{mL}$, illustrating that the HPDFZ NMs catalyzed H_2O_2 into $\bullet\text{OH}$ in a concentration-dependent manner, thus promoting MB degradation. Importantly, as revealed in Fig. S7, in the presence of GSH and H_2O_2 , the fluorescence intensity of THA in PFZ NM solution at pH 5.0 for 24 h was appreciably higher than that of THA in FZ NM solution at the same pH. Apparently, compared to FZ NMs, the PFZ NMs prominently reduced GSH-elicited $\bullet\text{OH}$ scavenging by the PDA-mediated GSH depletion, thus promoting $\bullet\text{OH}$ accumulation. According to these findings, the HPDFZ NMs were demonstrated to remarkably convert H_2O_2 to $\bullet\text{OH}$ in an acidity-triggered manner and consume GSH, thus reducing $\bullet\text{OH}$ scavenging by GSH (Fig. 4f). Therefore, it was expected that the HPDFZ NMs internalized by cancer cells can efficiently catalyze endogenous H_2O_2 to generate $\bullet\text{OH}$ and exhaust intracellular GSH to boost anticancer efficacy of CDT.

3.5. In vitro cellular uptake, intracellular $\bullet\text{OH}$ generation, mitochondria damage and LPO generation

In view of the active targeting of HA segments to CD44 on the membrane of cancer cells [46,47,63], the in vitro cellular uptake of HPDFZ NMs by CD44-overexpressed CT26 cells was evaluated by flow

cytometry and CLSM to explore their CD44-targeting performance. The intracellular DOX fluorescence intensity was employed as a quantity for the HPDFZ NMs internalization by CT26 cells. As presented in Fig. 5a and b, with the incubation time being prolonged from 1 to 4 h, CT26 cells incubated with HPDFZ NMs alone showed appreciably enhanced DOX fluorescence intensity compared to cells receiving HPDFZ NMs and free HA segments. Also, the CLSM images revealed that the uptake of HPDFZ NMs by CT26 cells pretreated with free HA segments was remarkably impeded, as reflected by the declined DOX fluorescence intensity within the cytoplasm (Fig. 5c and Fig. S8). Such a declined internalization of HPDFZ NMs by the HA-pretreated CT26 cells could be resulted from the competition of free HA segments with HPDFZ NMs for CD44 receptors of CT26 cells. Based on these findings, it was strongly demonstrated that the HPDFZ NMs can be efficiently internalized by CT26 cells via CD44-mediated endocytosis. Notably, the DOX fluorescence intensity of CT26 cells treated with HPDFZ NMs for 4 h, as shown in Fig. 5a, b, and c, is even higher than that of cells incubated with free DOX molecules despite different cellular pathways between HPDFZ NMs (CD44-mediated endocytosis) and free DOX (passive diffusion across cell membrane). This may be ascribed to that the CD44 receptor-mediated endocytosis of HPDFZ NMs could bypass the nature of DOX resistance of CT26 cells, thus promoting intracellular drug accumulation. Similar results that the nanovehicles conjugated with ligands or antibodies for active targeting realized efficient cellular uptake and increased drug retention in multidrug resistance (MDR) cancer cells via receptor-mediated endocytosis while avoiding P-glycoprotein (P-gp)-mediated drug efflux have been reported [64,65].

Next, the intracellular GSH level of CT26 cells incubated with HPDFZ NMs, FZ NMs, or Z NMs for 6 h was measured by DTNB assay to evaluate the GSH depletion ability of these NMs. As revealed in Fig. 5d, the intracellular GSH level of CT26 cells treated with FZ NMs determined to be ca 68.5 % is markedly lower than that (ca 90.8 %) of cells incubated with Z NMs. This suggests that the FZ NMs can moderately consume intracellular GSH by Fenton reaction-mediated $\text{Fe}^{2+}/\text{Fe}^{3+}$ redox couples. Note that the intracellular GSH levels of CT26 cells exposed to HPDFZ NMs were further decreased compared to that of cells treated with FZ NMs. According to the above results, it was demonstrated that the HPDFZ NMs effectively consumed intracellular GSH through Michael reaction of the PDA layer with endogenous GSH combined with the $\text{Fe}^{2+}/\text{Fe}^{3+}$ redox couple.

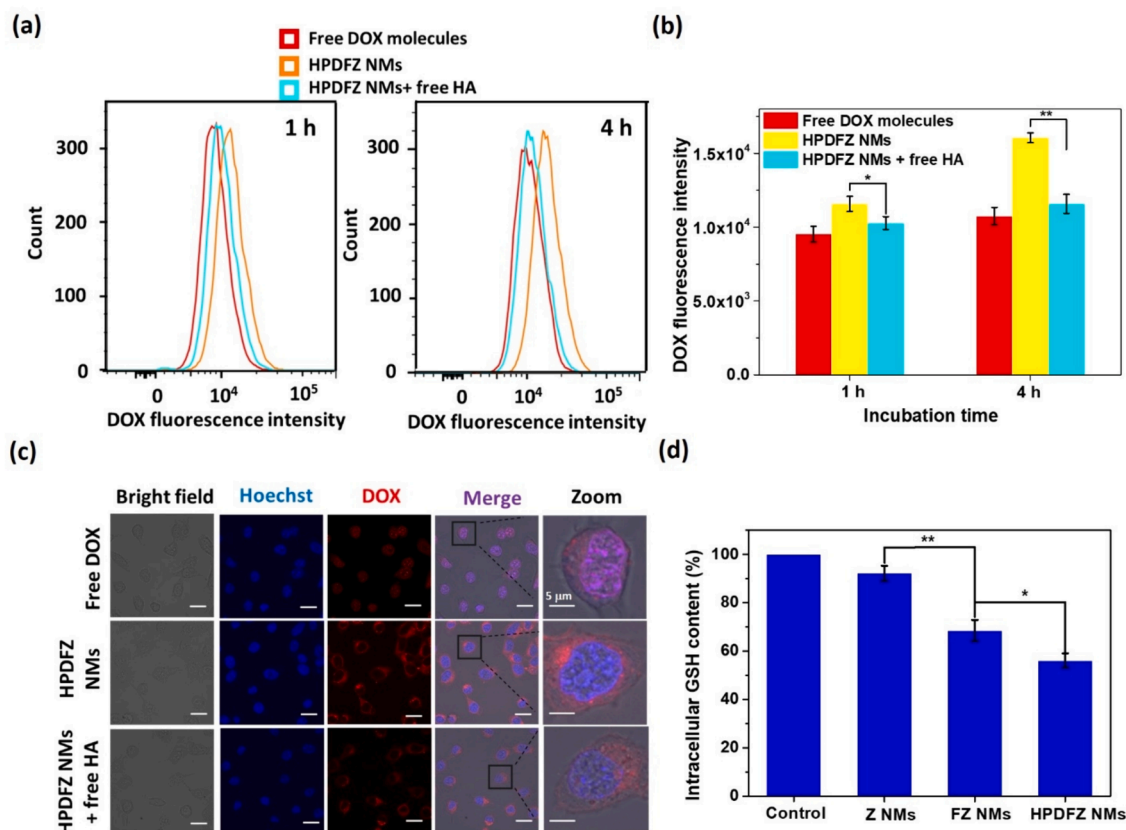


Fig. 5. (a) Flow cytometric histograms and (b) mean DOX fluorescence intensity of CT26 cells incubated with free DOX or HPDFZ NMs with or without free HA addition at 37 °C for 1 and 4 h (DOX concentration = 10 μM). (c) CLSM images of CT26 cells incubated with free DOX or HPDFZ NMs with or without free HA addition at 37 °C for 4 h (DOX concentration = 10 μM). Scale bars are 20 μm. (d) Intracellular GSH level of CT26 cells incubated with Z NMs, FZ NMs, and HPDFZ NMs, respectively, at 37 °C for 6 h.

In this study, the intracellular $\bullet\text{OH}$ generation capability of various NMs was assessed by DCFH-DA assay [66]. As shown in Fig. S9a and b, CT26 cells incubated with PFZ NMs exhibited appreciably strong DCF fluorescence relative to cells exposed to FZ NMs. As expected, compared to FZ NMs, the PFZ NMs could efficiently promote intracellular $\bullet\text{OH}$ accumulation by Fe^{2+} -mediated Fenton reaction combined with the reduced $\bullet\text{OH}$ scavenging upon PDA-mediated GSH depletion. Subsequently, to ensure a fair comparison of intracellular $\bullet\text{OH}$ generation performance among various NMs, the surfaces of Z NMs and FZ NMs were coated with PDA and HA to minimize the variances in cellular uptake. As shown in Fig. 6a and b, the intracellular DCF fluorescence of CT26 cells treated with either HPFZ or HPDFZ NMs was prominently higher than that of cells incubated with Fe^{2+} -free HPZ NMs or HPDZ NMs. This clearly illustrates that the HPFZ and HPDFZ NMs can efficiently catalyze endogenous H_2O_2 into $\bullet\text{OH}$ upon Fe^{2+} -mediated Fenton reaction, while the HPZ or HPDZ NMs cannot sufficiently degrade H_2O_2 due to poor Fenton catalytic activity of Zn^{2+} ions. Importantly, CT26 cells exposed to HPDFZ NMs showed a 30 % increase in DCF fluorescence intensity compared to cells receiving HPFZ NMs. Several studies pointed out that the intracellular DOX delivery could increase the local concentration of H_2O_2 [2,67,68]. Therefore, compared to DOX-free HPFZ NMs, the HPDFZ NMs internalized by CT26 cells could release DOX to generate H_2O_2 , thus enhancing the Fenton reaction together with Fe^{2+} ions to produce more $\bullet\text{OH}$.

Considering that the mitochondria damage is a crucial and representative mark of $\bullet\text{OH}$ -induced apoptosis [20,29,69], the effect of the HPDFZ NMs internalized by CT26 cells on the mitochondria was investigated by observing the depolarization of the mitochondria membranes with JC-1 kit. When the mitochondrial membrane potential decreases due to apoptosis, JC-1 transforms from the aggregate form

into a monomer, thus leading to a change of fluorescence from red to green [29,69]. As presented in Fig. 6c, no significant green fluorescence was observed in the control group, while weak green fluorescence signals were attained in CT26 cells incubated with free DOX molecules, HPZ, and HPDZ NMs, respectively, being indicative of minor damage of mitochondria. By contrast, the HPDFZ or HPFZ NMs-treated cells exhibited strong green fluorescence, illustrating severe disruption of mitochondria. Compared to the HPFZ NM group, the HPDFZ group displayed higher green fluorescence signals. Being corresponding to the results of intracellular $\bullet\text{OH}$ generation (Fig. 6a and b), the endocytosed HPDFZ NMs effectively promoted intracellular $\bullet\text{OH}$ accumulation via Fe^{2+} -mediated Fenton reaction in combination with dual GSH depletion, thus potently damaging mitochondria. The over-generation of intracellular $\bullet\text{OH}$ has been demonstrated to irreversibly oxidize the cellular unsaturated lipid, thus leading to ferroptosis, a type of iron-dependent non-apoptotic cell death [69,70]. To explore intracellular LPO product accumulation of CT26 cells treated with HPDFZ NMs, the BODIPY 581/591 C11 as an LPO sensor was utilized. As presented in Fig. 6d, CT26 cells incubated with HPDFZ NMs exhibited the strongest green fluorescence signal among cells receiving other treatments. This further suggests that the Fe^{2+} -mediated Fenton reaction and dual GSH depletion of the internalized HPDFZ NMs could prominently enhance $\bullet\text{OH}$ production, thereby boosting intracellular accumulation of toxic LPO products. Based on these findings, it was expected that the HPDFZ NMs could not only effectively promote intracellular DOX delivery but also largely disturb redox homeostasis, thus augmenting the anticancer effect of the combined CDT and CT (Scheme 1b).

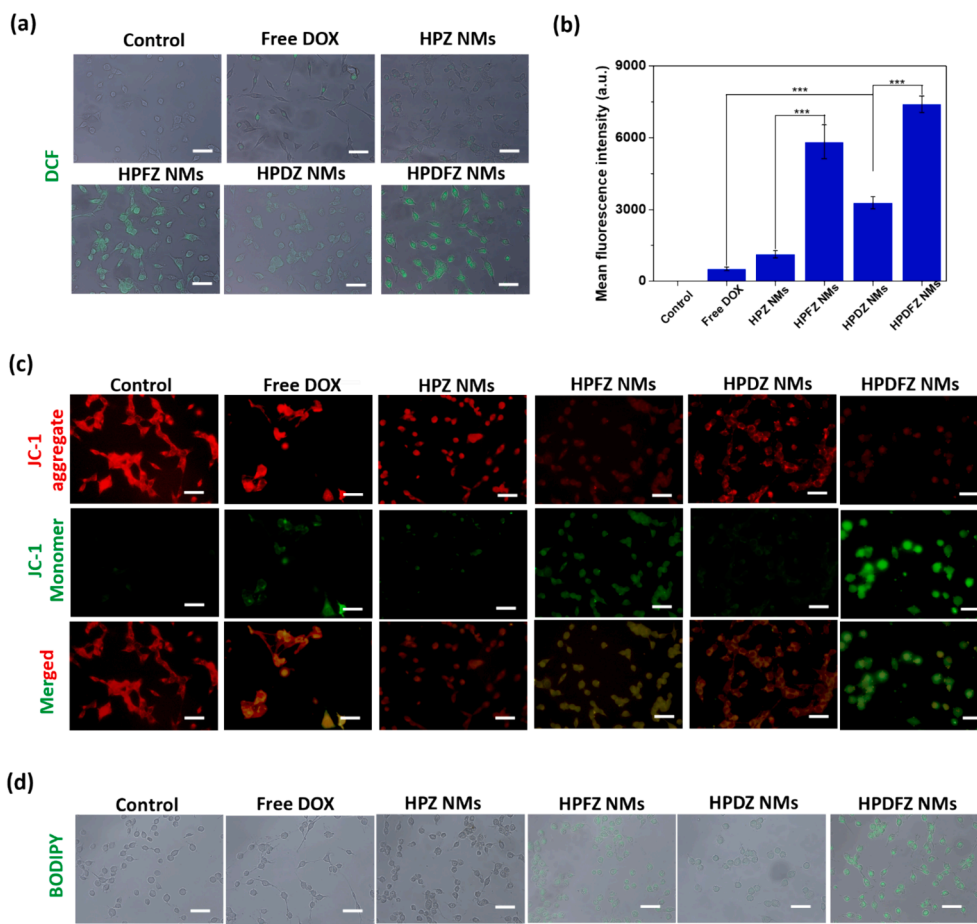


Fig. 6. (a) Fluorescence images and (b) quantified DCF fluorescence intensity of CT26 cells receiving different treatments for 6 h and stained with DCFH-DA for detection of intracellular $\bullet\text{OH}$ production. Scale bars are 50 μm . (c) Fluorescence images of CT26 cells receiving various treatments for 24 h and stained with JC-1 reagent for the measure of mitochondrial damage. Scale bars are 50 μm . (d) BODIPYTM 581/591 C11 staining of CT26 cells receiving various treatments for 24 h. Scale bars are 50 μm .

3.6. *In vitro* anticancer effect of combined CDT and CT

To evaluate the anticancer efficacy of DOX-based CT combined with Fe^{2+} -mediated CDT, the viability of CT26 cells treated with HPDFZ NMs was determined by MTT assay. As shown in Fig. 7a, the viability of CT26 cells treated with HPFZ NMs was appreciably reduced from 81.1 to 34.3 % in the NM concentration-dependent manner, while CT26 cells incubated with HPZ NMs retained mean viability above 70 % (Fig. 7a). Evidently, compared to HPZ NMs, the HPFZ NMs efficiently produced $\bullet\text{OH}$ via Fe^{2+} -mediated Fenton reaction, thereby eliciting massive mitochondrial damage and LPO to provoke cell apoptosis and ferroptosis. Notably, at the same DOX or NM concentration, the HPDFZs exhibited higher cytotoxicity against CT26 cells than HPDZ NMs and HPFZ NMs. Also, the fluorescence staining of live/dead CT26 cells showed that most of CT26 cells treated with HPDFZ NMs displayed considerably PI-positive staining as compared to cells receiving HPZ, HPFZ or HPDZ NMs (Fig. 7b). These data clearly demonstrate that the combination of DOX chemotherapy and Fe^{2+} -involved CDT delivered by HPDFZ NMs could effectively kill cancer cells in comparison with single CT of HPDZ NMs or CDT of HPFZ NMs. Also, the IC_{50} value of HPDFZ NMs attained to be ca. 2.9 μM is lower relative to that (9.3 μM) of HPDZ NMs and that (4.3 μM) of free DOX molecules (Fig. 7c), indicating that the HPDFZ NMs could realize a low DOX dosage but effective anticancer efficacy against CT26 cells, mainly due to CD44-targeted delivery of the combined CDT and CT. On the other hand, similar findings that the HPDFZ NMs displayed the capability of killing cancer cells superior to HPDZ NMs and HPFZ NMs by the combination of CDT and CT were also

obtained in another cell model, TRAMP-C1 cancer cells (Fig. 7d). It should be mentioned that different from CT26 cells, TRAMP-C1 cells treated with free DOX molecules showed significantly reduced viability compared to cells receiving HPDFZ NPs. This may be ascribed to that TRAMP-C1 cells are more sensitive to DOX than CT26 cells. The colon cancer cells have been found to have high levels of P-gp, an ATP-binding cassette transporter that contributes to MDR [71,72]. This over-expression occurs on the cell and nuclear membranes, resulting in a high IC_{50} value for free DOX against CT26 cancer cells [71,72]. On the other hand, the HPFZ NMs (7.8 ~ 125 $\mu\text{g}/\text{mL}$) showed quite low cytotoxicity on the healthy WS1 cells, human skin fibroblast cells, as evidenced by relatively high viability of WS1 cells (beyond 90 %) (Fig. S10). The results further verify that the CDT delivered by HPFZ NMs specifically kills cancer cells rather than normal cells because H_2O_2 is overexpressed in cancer cells compared with normal cells, thus amplifying Fenton reaction-mediated $\bullet\text{OH}$ production within cancer cells.

3.7. *In vivo* biodistribution and tumor accumulation

Considering the poor NIR fluorescence of DOX and nonnegligible autofluorescence of BALB/c mice, the amphiphilic IR820, a NIR dye, instead of DOX, was encapsulated into HPFZ NMs for observing the *in vivo* biodistribution of NMs using fluorescence imaging. Through the π - π stacking and hydrophobic interactions of IR820 with PDA layer of HPFZ NMs, IR820 molecules were incorporated into HPFZ NMs. As presented in Fig. S11, the IR820@HPFZ NMs exhibited enhanced absorption from 600 to 900 nm compared to HPFZ NMs, confirming the successful

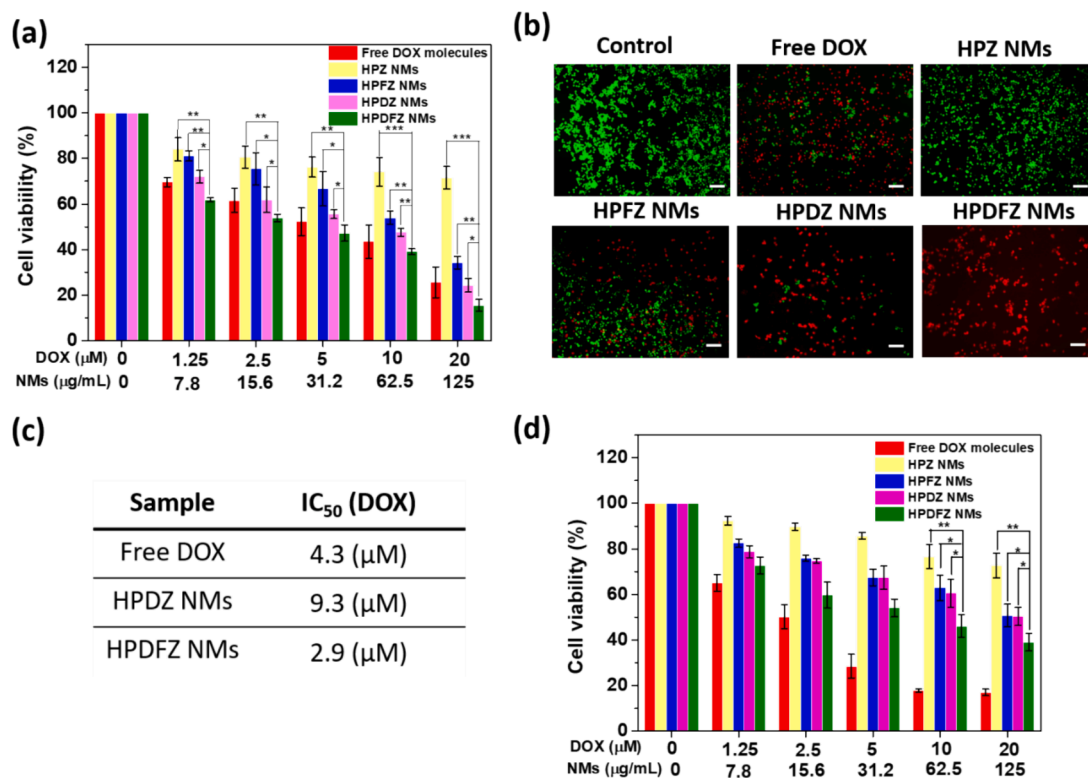


Fig. 7. (a) Cell viability and (b) calcein-AM/PI-staining of CT26 cells receiving different treatments at 37 °C for 24 h. The viable cells were stained green with calcein-AM, and the dead cells were stained red with PI. Scale bars are 200 μm. (c) IC₅₀ values of free DOX, HPDZ NMs, and HPDFZ NMs on CT26 cells. (d) Cell viability of TRAMP-C1 cells receiving different treatments at 37 °C for 24 h. (For interpretation of the references to color in this figure legend, the reader is referred to the web version of this article.)

encapsulation of IR820 into HPFZ NMs. Also, the particle size of IR820@HPFZ NMs was determined to be ca 276.7 nm, being slightly larger than that of HPFZ NMs. Upon intravenous injection with

IR820@HPFZs or free IR820 molecules as the control, the in vivo IR820 fluorescence images of CT26 tumor-bearing mice were attained at different time intervals. Notably, compared to the free IR820 group, the

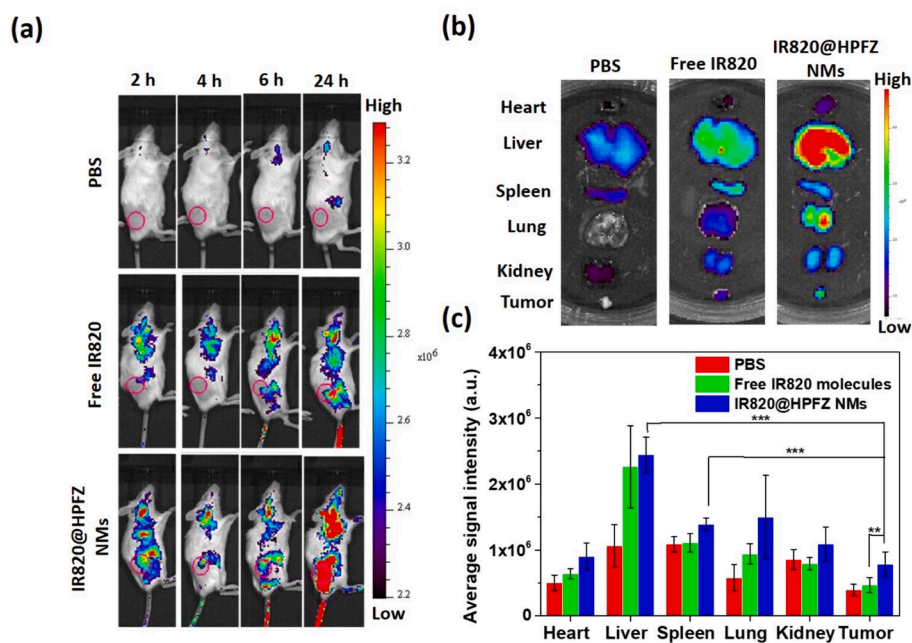


Fig. 8. (a) In vivo NIR fluorescence images of CT26 tumor-bearing mice receiving intravenous injection of free IR820 molecules or IR820@HPFZ NMs attained by IVIS. The tumor sites were marked with pink circle. (b) NIR fluorescence images of the isolated major organs and tumors at 24 h post-injection with different IR820-containing formulations. (c) Average IR820 fluorescence intensities of individual organs and tumor from CT26 tumor-bearing mice treated with free IR820 molecules or IR820@HPFZ NMs. (For interpretation of the references to color in this figure legend, the reader is referred to the web version of this article.)

IR820@HPFZ NM group showed visibly higher IR820 fluorescence intensity in the tumor sites during the identical period (Fig. 8a). Moreover, the ex vivo fluorescence intensity of tumors receiving IR820@HPFZ NMs at 24 h post-injection was remarkably stronger than that of tumors from free IR820 groups (Fig. 8b and c). Based on these data, obviously, compared to small-molecule IR820 with poor tumor deposition due to lack of tumor specificity, the IR820@HPFZ NMs exhibited promoted tumor accumulation by the enhanced permeability and retention (EPR) effect and HA-mediated CD44 targeting. However, due to inevitable nanoparticle capture by the reticuloendothelial system, the ex vivo IR820 fluorescence signals of the liver and spleen of tumor-bearing mice treated with IR820@HPFZ NMs were much higher in comparison with that of the tumor. Similar biodistribution of payload-carrying nanoparticles in tumor-bearing mice has been observed in other studies [73–76].

3.8. In vivo tumor growth suppression by combined CDT and CT

Inspired by the prominent in vitro anticancer effect of HPDFZ NMs on CT26 cells, we further evaluated their CDT/CT-mediated antitumor potency in the CT26 xenograft mouse model in vivo (Fig. 9a). The change of tumor volume and body weight of CT26 tumor-bearing mice receiving different treatments were recorded for up to 18 days post first intravenous injection. As revealed in Fig. 9b, the tumor volumes of mice

treated with HPDZ NMs were only slightly smaller than those of mice receiving PBS as the control during the treatment process, indicating the failure of a single DOX-mediated CT in inhibiting tumor growth. Compared to HPDZ NMs, the HPFZ NMs exhibited a limited suppression on tumor growth over the period of 10 days post-treatment, beyond which tumors receiving this formulation gradually enlarged. Notably, 18 days after treatment, the tumor volume of mice treated with HPDFZ NMs was much smaller than that of mice receiving either HPFZ NMs or HPDZ NMs. Moreover, despite that free DOX molecules were administered at a total dose 1.5 times higher than the DOX dose of HPDFZ NMs, the former still showed appreciably lower antitumor effectiveness compared to the latter. In line with the results of in vivo tumor growth inhibition, tumors collected from the sacrificed mice treated with HPDFZ NMs showed the smallest weight and size compared to tumors receiving other treatments (Fig. 9c and d). These findings suggest that the HA-mediated CD44-targeted CDT and CT of HPDFZ NMs potentially inhibited tumor growth at low DOX dose as compared to free DOX molecules. Besides, the treated mice in all groups maintained virtually unvaried body weight (Fig. S12), revealing that the single CDT, DOX-based CT, or the related combined therapy did not elicit severe acute toxicity.

As shown in the H&E staining images of the tumor sections (Fig. 9e), the HPDFZ NM group exhibited lower cell density and more nuclear fragmentation in comparison with other treatment groups. Also, an

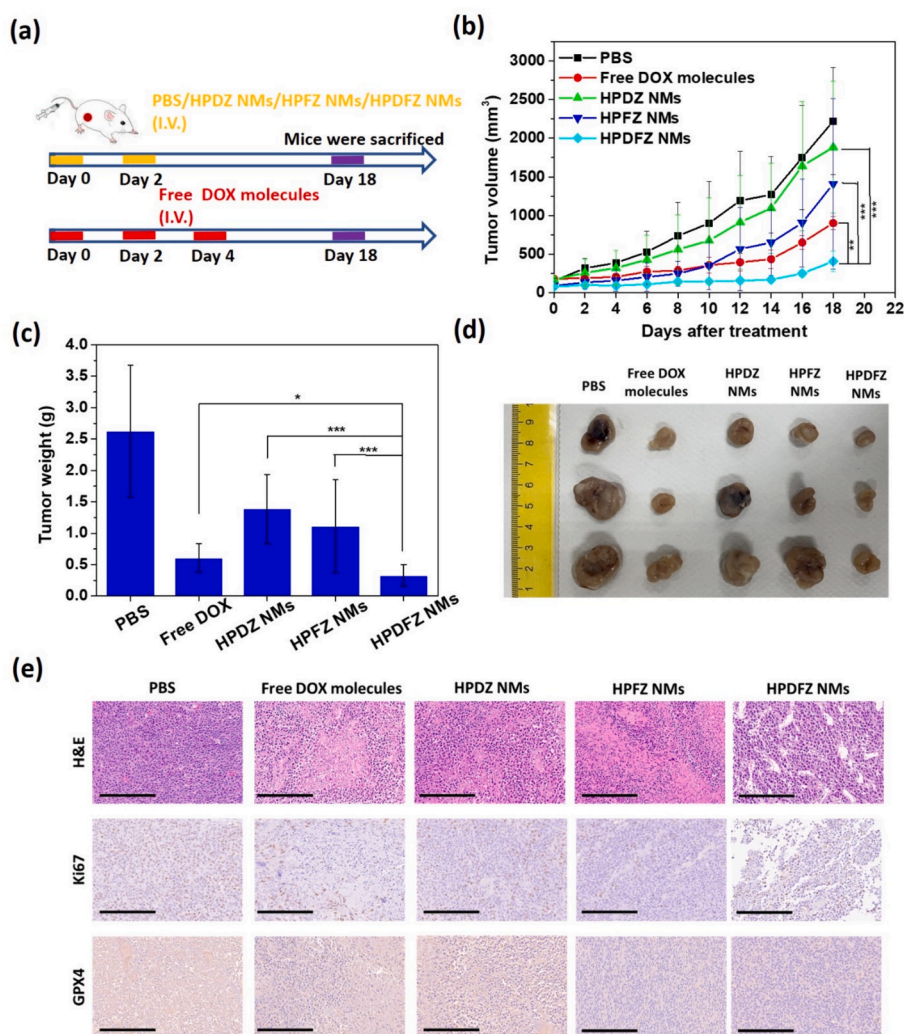


Fig. 9. (a) Experimental flowchart of in vivo tumor growth inhibition study. (b) Tumor growth inhibition profiles of CT26 tumor-bearing mice receiving different treatments. (c) Weight and (d) photographs of the tumors harvested from the euthanized mice at day 18 after the treatment. (e) H&E, Ki-67 and GPX4 staining of tumor slides from CT26 tumor-bearing mice receiving different treatments. Scale bars are 200 μm.

appreciable reduction in Ki67 proliferation staining was attained in the tumor sections of HPDFZ NM group. These results further illustrate that the combined CDT and CT delivered by HPDFZ NMs can execute potent anti-proliferative effects. Additionally, the GPX4-stained images revealed that the tumor sections of mice treated with HPDFZ or HPFZ NMs displayed largely decreased expression of GPX4 compared to those of other treatment groups. This could be attributed to that the HPDFZ and HPFZ NMs can effectively consume GSH of tumor cells by $\text{Fe}^{2+}/\text{Fe}^{3+}$ -based redox couple and PDA-mediated Michael reaction, thereby inducing GPX4 inactivation. As observed in some previous studies [2,7,10], when the activity of GPX4 in cancer cells was inhibited, the capability of the tumor to scavenge $\bullet\text{OH}$ was appreciably declined, thus promoting LPO to elicit ferroptosis. Note that no appreciable abnormality was observed in the major organs of mice receiving different treatments (Fig. S13). In view of these findings, it can be verified that the HPDFZ NMs designed in this work not only actively target CD44-overexpressed tumor but also effectively realize intracellular DOX delivery and destroy redox homeostasis by promoting $\bullet\text{OH}$ production and GSH depletion, thus leading to intracellular mitochondrial damage and LPO (Scheme 1b). Therefore, through the combination of CDT-triggered ferroptosis and CT-mediated apoptosis, the HPDFZ NMs potently inhibited tumor growth at low DOX dose without significant systemic toxicity.

4. Conclusions

To potentially enhance antitumor potency by the active tumor-targeted combined CDT and CT, the FZ NMs were fabricated, sequentially decorated with PDA and HA, and employed as DOX vehicles. Different from the previously reported FZ NMs [42,43], the HPDFZ NMs designed in this study not only effectively consumed GSH by the PDA-mediated Michael addition combined with $\text{Fe}^{2+}/\text{Fe}^{3+}$ redox couple but also showed CD44-targeting capability. Also, the HPDFZ NMs exhibited prominent colloidal stability in the FBS-containing culture medium and accelerated DOX and Fe^{2+} release under GSH-rich and weakly acidic conditions. Moreover, the HPDFZ NMs promoted the degradation of H_2O_2 into $\bullet\text{OH}$ in response to pH reduction from 7.4 to 5.0. After being internalized by CT26 cells via CD44-mediated endocytosis, the HPDFZ NMs sufficiently generated $\bullet\text{OH}$, depleted GSH, and released DOX, thus leading to cell apoptosis and ferroptosis upon the combination of CDT and CT. The in vivo animal studies further verified that the CD44-targeting HPDFZ NMs efficiently accumulated within the CT26 tumor and significantly inhibited tumor growth with a satisfied biocompatibility. Overall, the versatile HPDFZ NMs developed in this work can realize the tumor-targeted and GSH depletion-boosted CDT/CT combined therapy, thus showing great promise in future catalytic tumor-specific treatment.

CRedit authorship contribution statement

Kai-An Liang: Project administration, Methodology, Investigation, Formal analysis, Data curation. **Hsiang-Yun Chih:** Visualization, Validation, Methodology, Investigation, Formal analysis. **I-Ju Liu:** Visualization, Validation, Methodology, Investigation, Formal analysis. **Nien-Tzu Yeh:** Visualization, Software, Investigation, Formal analysis. **Tsai-Ching Hsu:** Supervision, Resources, Investigation. **Hao-Yang Chin:** Visualization, Methodology, Formal analysis. **Bor-Show Tzang:** Writing – original draft, Supervision, Resources, Investigation, Funding acquisition. **Wen-Hsuan Chiang:** Writing – review & editing, Writing – original draft, Supervision, Investigation, Funding acquisition, Data curation, Conceptualization.

Declaration of competing interest

The authors declare that they have no known competing financial interests or personal relationships that could have appeared to influence

the work reported in this paper.

Data availability

Data will be made available on request.

Acknowledgments

This work is supported by the National Science and Technology Council (MOST 111-2628-E-005-009-MY2; NSTC 113-2628-E-005-002-MY3), National Chung Hsing University and Chung Shan Medical University (NCHU-CSMU 11202), Taiwan.

Appendix A. Supplementary data

Supplementary data to this article can be found online at <https://doi.org/10.1016/j.jcis.2024.07.241>.

References

- [1] L. Wang, Y. Xu, C. Liu, W. Si, W. Wang, Y. Zhang, L. Zhong, X. Dong, Y. Zhao, Copper-doped MOF-based nanocomposite for GSH depleted chemo/photothermal/chemodynamic combination therapy, *Chem. Eng. J.* 438 (2022) 135567.
- [2] X. Fu, Y. Zhang, G. Zhang, X. Li, S. Ni, J. Cui, Targeted delivery of fenton reaction packages and drugs for cancer theranostics, *Appl. Mater. Today* 26 (2022) 101353.
- [3] M.R. Saeb, N. Rabiee, M. Mozafari, F. Verpoort, L.G. Voskressensky, R. Luque, Metal-organic frameworks (MOFs) for cancer therapy, *Materials (Basel)* 14 (2021) 7277.
- [4] W.X. Zhang, Y.N. Hao, Y.R. Gao, Y. Shu, J.H. Wang, Mutual benefit between Cu(II) and polydopamine for improving photothermal-chemodynamic therapy, *ACS Appl. Mater. Interfaces* 13 (2021) 38127.
- [5] X. Di, Z. Pei, Y. Pei, T.D. James, Tumor microenvironment-oriented MOFs for chemodynamic therapy, *Coord. Chem. Rev.* 484 (2023) 215098.
- [6] B. Wang, Y. Dai, Y. Kong, W. Du, H. Ni, H. Zhao, Z. Sun, Q. Shen, M. Li, Q. Fan, Tumor microenvironment-responsive Fe(III)-porphyrin nanotheranostics for tumor imaging and targeted chemodynamic-photodynamic therapy, *ACS Appl. Mater. Interfaces* 12 (2020) 53634.
- [7] H. Deng, J. Zhang, Y. Yang, J. Yang, Y. Wei, S. Ma, Q. Shen, Chemodynamic and photothermal combination therapy based on dual-modified metal-organic framework for inducing tumor ferroptosis/pyroptosis, *ACS Appl. Mater. Interfaces* 14 (2022) 24089.
- [8] X.X. Yang, X. Xu, M.F. Wang, H.Z. Xu, X.C. Peng, N. Han, T.T. Yu, L.G. Li, Q.R. Li, X. Chen, Y. Wen, T.F. Li, A nanoreactor boosts chemodynamic therapy and ferroptosis for synergistic cancer therapy using molecular amplifier dihydroartemisinin, *J. Nanobiotechnology* 20 (2022) 230.
- [9] X. Meng, X. Zhang, M. Liu, B. Cai, N. He, Z. Wang, Fenton reaction-based nanomedicine in cancer chemodynamic and synergistic therapy, *Appl. Mater. Today* 21 (2020) 100864.
- [10] X. Zhang, S. Lin, F. Zhao, J. Zhang, S. Lei, F. Bai, Q. Liu, J. Wu, T. He, P. Huang, J. Lin, Programmably controllable delivery of metastable ferrous ions for multiscale dynamic imaging guided photothermal primed chemodynamic therapy, *Adv. Mater.* 35 (2023) 2210876.
- [11] C. Li, Y. Wan, Y. Zhang, L.H. Fu, N.T. Blum, R. Cui, B. Wu, R. Zheng, J. Lin, Z. Li, P. Huang, In situ sprayed starvation/chemodynamic therapeutic gel for post-surgical treatment of IDH1 (R132H) glioma, *Adv. Mater.* 34 (2022) 2103980.
- [12] X. Zhang, Q. Qu, A. Yang, J. Wang, W. Cheng, Y. Deng, A. Zhou, T. Lu, R. Xiong, C. Huang, Chitosan enhanced the stability and antibiofilm activity of self-propelled Prussian blue micromotor, *Carbohydr. Polym.* 299 (2023) 120134.
- [13] T. Lu, W. Cao, H. Liang, Y. Deng, Y. Zhang, M. Zhu, W. Ma, R. Xiong, C. Huang, Blow-spun nanofibrous membrane for simultaneous treatment of emulsified oil/water mixtures, dyes, and bacteria, *Langmuir* 38 (2022) 15729–15739.
- [14] C. Liu, Y. Cao, Y. Cheng, D. Wang, T. Xu, L. Su, X. Zhang, H. Dong, An open source and reduce expenditure ROS generation strategy for chemodynamic/photodynamic synergistic therapy, *Nat. Commun.* 11 (2020) 1735.
- [15] B. Liu, Y. Bian, S. Liang, M. Yuan, S. Dong, F. He, S. Gai, P. Yang, Z. Cheng, J. Lin, One-step integration of tumor microenvironment-responsive calcium and copper peroxides nanocomposite for enhanced chemodynamic/ion-interference therapy, *ACS Nano* 16 (2022) 617.
- [16] Y. Sun, Y. Wang, Y. Liu, B. Weng, H. Yang, Z. Xiang, J. Ran, H. Wang, C. Yang, Intelligent tumor microenvironment-activated multifunctional nanoplateform coupled with turn-on and always-on fluorescence probes for imaging-guided cancer treatment, *ACS Appl. Mater. Interfaces* 13 (2021) 53646.
- [17] T.H. Wang, M.Y. Shen, N.T. Yeh, Y.H. Chen, T.C. Hsu, H.Y. Chin, Y.T. Wu, B. S. Tzang, W.H. Chiang, Photothermal nanozymes to self-augment combination cancer therapy by dual-glutathione depletion and hyperthermia/acidity-activated hydroxyl radical generation, *J. Colloid Interface Sci.* 650 (2023) 1698.
- [18] S. Hao, J. Zuo, H. Huang, W. Li, H. Guo, M. Liu, H. Zhu, H. Sun, Enzyme functionalized PEOz modified magnetic polydopamine with enhanced penetration for cascade-augmented synergistic tumor therapy, *Int. J. Biol. Macromol.* 242 (2023) 124048.

- [19] C. Wu, D. Xu, M. Ge, J. Luo, L. Chen, Z. Chen, Y. You, Y.X. Zhu, H. Lin, J. Shi, Blocking glutathione regeneration: inorganic NADPH oxidase nanozyme catalyst potentiates tumoral ferroptosis, *Nano Today* 46 (2022) 101574.
- [20] Z. Liu, S. Liu, B. Liu, Y. Bian, M. Yuan, C. Yang, Q. Meng, C. Chen, P. Ma, J. Lin, Fe (III)-naphthazarin metal-phenolic networks for glutathione-depleting enhanced ferroptosis-apoptosis combined cancer therapy, *Small* 19 (2023) 2207825.
- [21] L. Zhang, Y. Fan, Z. Yang, M. Yang, C.Y. Wong, NIR-II-driven and glutathione depletion-enhanced hypoxia-irrelevant free radical nanogenerator for combined cancer therapy, *J. Nanobiotechnology* 19 (2021) 265.
- [22] Z. Xiao, W. Zuo, L. Chen, L. Wu, N. Liu, J. Liu, Q. Jin, Y. Zhao, X. Zhu, H₂O₂ Self-supplying and GSH-depleting nanoplatfor for chemodynamic therapy synergetic photothermal/chemotherapy, *ACS Appl Mater Interfaces* 13 (2021) 43925.
- [23] Y. Zeng, H. Zhou, J. Ding, W. Zhou, Cell membrane inspired nano-shell enabling long-acting glucose oxidase for melanoma starvation therapy via microneedles-based percutaneous delivery, *Theranostics* 11 (2021) 8270.
- [24] Y. Li, Z. Liu, W. Zeng, Z. Wang, C. Liu, N. Zeng, K. Zhong, D. Jiang, Y. Wu, A novel H₂O₂ generator for tumor chemotherapy-enhanced CO gas therapy, *Front. Oncol.* 11 (2021) 738567.
- [25] Y. Wu, Y. Li, G. Lv, W. Bu, Redox dyshomeostasis strategy for tumor therapy based on nanomaterials chemistry, *Chem. Sci.* 13 (2022) 2202.
- [26] J. Xin, C. Deng, O. Aras, M. Zhou, C. Wu, F.J. An, Chemodynamic nanomaterials for cancer theranostics, *Nanobiotechnology* 19 (2021) 192.
- [27] X. Zhang, H. Guo, X. Zhang, X. Shi, P. Yu, S. Jia, C. Cao, S. Wang, J. Chang, Dual-prodrug cascade activation for chemo/chemodynamic mutually beneficial combination cancer therapy, *Biomater. Sci.* 11 (2023) 1066.
- [28] Y. Guo, X. Zhang, W. Sun, H.R. Jia, Y.X. Zhu, X. Zhang, N. Zhou, F.G. Wu, Metal-phenolic network-based nanocomplexes that evoke ferroptosis by apoptosis: promoted nuclear drug influx and reversed drug resistance of cancer, *Chem. Mater.* 31 (2019) 10071.
- [29] K. Sun, J. Yu, J. Hu, W. Yang, X. Chu, L. Chen, X. Deng, B. Sun, Z. Wang, Photothermal enhanced polyphenol-based nanofibers ameliorate catalytic efficiency of ferroptosis for synergistic tumor therapy, *Chem. Eng. J.* 470 (2023) 144360.
- [30] J. Yang, H. Yao, Y. Guo, B. Yang, J. Shi, Enhancing tumor catalytic therapy by co-catalysis, *Angew. Chem. Int. Ed.* 61 (2022) 202200480.
- [31] Y. Deng, T. Lu, J. Cui, S.K. Samal, R. Xiong, C. Huang, Bio-based electrospun nanofiber as building blocks for a novel eco-friendly air filtration membrane: A review, *Sep. Purif. Technol.* 277 (2021) 119623.
- [32] Q. Fan, T. Lu, Y. Deng, Y. Zhang, W. Ma, R. Xiong, C. Huang, Bio-based materials with special wettability for oil-water separation, *Sep. Purif. Technol.* 297 (2022) 121445.
- [33] W. Cao, M. Zhang, W. Ma, C. Huang, Multifunctional electrospun nanofibrous membrane: an effective method for water purification, *Sep. Purif. Technol.* 327 (2023) 124952.
- [34] T. Lu, H. Liang, W. Cao, Y. Deng, Q. Qu, W. Ma, R. Xiong, C. Huang, Blow-spun nanofibrous composite Self-cleaning membrane for enhanced purification of oily wastewater, *J. Colloid Interface Sci.* 608 (2022) 2860–2869.
- [35] B.N. Yalamandala, W.T. Shen, S.H. Min, W.H. Chiang, S.J. Chang, S.H. Hu, Advances in functional metal-organic frameworks based on-demand drug delivery systems for tumor therapeutics, *Adv. Nanobiomed Res.* 1 (2021) 2100014.
- [36] J. Liu, Y. Yuan, Y. Cheng, D. Fu, Z. Chen, Y. Wang, L. Zhang, C. Yao, L. Shi, M. Li, C. Zhou, M. Zou, G. Wang, L. Wang, Z. Wang, Copper-based metal-organic framework overcomes cancer chemoresistance through systemically disrupting dynamically balanced cellular redox homeostasis, *J. Am. Chem. Soc.* 144 (2022) 4799.
- [37] J. Chen, Y. Wang, H. Niu, Y. Wang, A. Wu, C. Shu, Y. Zhu, Y. Bian, K. Lin, Metal-organic framework-based nanoagents for effective tumor therapy by dual dynamics-amplified oxidative stress, *ACS Appl. Mater. Interfaces* 13 (2021) 45201.
- [38] H. Liu, C. Xu, M. Meng, S. Li, S. Sheng, S. Zhang, W. Ni, H. Tian, Q. Wang, Metal-organic framework-mediated multifunctional nanoparticles for combined chemophotothermal therapy and enhanced immunotherapy against colorectal cancer, *Acta Biomater.* 144 (2022) 132.
- [39] F. Liu, L. Lin, Y. Zhang, Y. Wang, S. Sheng, C. Xu, H. Tian, X. Chen, A tumor-microenvironment-activated nanozyme-mediated theranostic nanoreactor for imaging-guided combined tumor therapy, *Adv. Mater.* 31 (2019) 1902885.
- [40] Y. Wang, J. Yan, N. Wen, H. Xiong, S. Cai, Q. He, Y. Hu, D. Peng, Z. Liu, Y. Liu, Metal-organic frameworks for stimuli-responsive drug delivery, *Biomaterials* 230 (2020) 119619.
- [41] K.S. Park, Z. Ni, A.P. Côté, J.Y. Choi, R. Huang, F.J. Uribe-Romo, H.K. Chae, M. O’Keeffe, O.M. Yaghi, Exceptional chemical and thermal stability of zeolitic imidazolate frameworks, *Proc. Natl. Acad. Sci. U S A.* 103 (2006) 10186.
- [42] H. Chu, J. Shen, C. Wang, Y. Wei, Biodegradable iron-doped ZIF-8 based nanotherapeutic system with synergistic chemodynamic/photothermal/chemotherapy, *Colloids Surf. a: Physicochem. Eng. Asp.* 628 (2021) 127388.
- [43] Y. Zhong, Z. Peng, Y. Peng, B. Li, Y. Pan, Q. Ouyang, H. Sakiyama, M. Muddassar, J. Liu, Construction of Fe-doped ZIF-8/DOX nanocomposites for ferroptosis strategy in the treatment of breast cancer, *J. Mater. Chem. B* 11 (2023) 6335.
- [44] K. Lu, T. Aung, N. Guo, R. Weichselbaum, W. Lin, Nanoscale metal-organic frameworks for therapeutic, imaging, and sensing applications, *Adv. Mater.* 30 (2018) 1707634.
- [45] J. Xiao, L. Hai, Y. Li, H. Li, M. Gong, Z. Wang, Z. Tang, L. Deng, D. He, An ultrasmall Fe₃O₄-decorated polydopamine hybrid nanozyme enables continuous conversion of oxygen into toxic hydroxyl radical via GSH-depleted cascade redox reactions for intensive wound disinfection, *Small* 18 (2022) 2105465.
- [46] L. Zhong, L. Xu, Y. Liu, Q. Li, D. Zhao, Z. Li, H. Zhang, H. Zhang, Q. Kan, Y. Wang, J. Sun, Z. He, Transformative hyaluronic acid-based active targeting supramolecular nanoplatfor improves long circulation and enhances cellular uptake in cancer therapy, *Acta Pharm. Sin. b.* 9 (2019) 397.
- [47] Q. Sun, H. Bi, Z. Wang, C. Li, X. Wang, J. Xu, H. Zhu, R. Zhao, F. He, S. Gai, P. Yang, Hyaluronic acid-targeted and pH-responsive drug delivery system based on metal-organic frameworks for efficient antitumor therapy, *Biomaterials* 223 (2019) 119473.
- [48] Y. Zhang, H. Xiao, R. Xiong, C. Huang, Xylan-based ratiometric fluorescence carbon dots composite with delignified wood for highly efficient water purification and photothermal conversion, *Sep. Purif. Technol.* 324 (2023) 124513.
- [49] Y. Deng, T. Lu, X. Zhang, Z. Zeng, R. Tao, Q. Qu, Y. Zhang, M. Zhu, R. Xiong, C. Huang, Hierarchical fiber with granular-convex structure for highly efficient PM_{2.5} capture, *Sep. Purif. Technol.* 304 (2023) 122235.
- [50] Y. Deng, T. Lu, X. Zhang, Z. Zeng, R. Tao, Q. Qu, Y. Zhang, M. Zhu, R. Xiong, C. Huang, Multi-hierarchical nanofiber membrane with typical curved-ribbon structure fabricated by green electrospinning for efficient, breathable and sustainable air filtration, *J. Membr. Sci.* 660 (2022) 120857.
- [51] J. Cui, T. Lu, F. Li, Y. Wang, J. Lei, W. Ma, Y. Zou, C. Huang, Flexible and transparent composite nanofibre membrane that was fabricated via a “green” electrospinning method for efficient particulate matter 2.5 capture, *J. Colloid Interface Sci.* 582 (2021) 506–514.
- [52] Q. Qu, A. Yang, J. Wang, M. Xie, X. Zhang, D. Huang, R. Xiong, D. Pei, C. Huang, Responsive and biocompatible chitosan-phytate microparticles with various morphology for antibacterial activity based on gas-shearing microfluidics, *J. Colloid Interface Sci.* 649 (2023) 68–75.
- [53] S. Li, W. Zhang, R. Xing, C. Yuan, H. Xue, X. Yan, Supramolecular nanofibrils formed by coassembly of clinically approved drugs for tumor photothermal immunotherapy, *Adv. Mater.* 33 (2021) 2100595.
- [54] C. Li, J. Ye, X. Yang, S. Liu, Z. Zhang, J. Wang, K. Zhang, J. Xu, Y. Fu, P. Yang, Fe/Mn bimetal-doped ZIF-8-coated luminescent nanoparticles with up/downconversion dual-mode emission for tumor self-enhanced NIR-II imaging and catalytic therapy, *ACS Nano* 16 (2022) 18143.
- [55] J.T. Luo, Y.C. Yang, X.Y. Zhu, G. Chen, F. Zeng, F. Pan, Enhanced electromechanical response of Fe-doped ZnO films by modulating the chemical state and ionic size of the Fe dopant, *Phys. Rev. B* 82 (2010) 014116.
- [56] L.E. Mphuthi, E. Erasmus, E.H.G. Langner, Metal exchange of ZIF-8 and ZIF-67 nanoparticles with Fe(II) for enhanced photocatalytic performance, *ACS Omega* 6 (2021) 31632–31645.
- [57] R. Foroutan, S.J. Peighambaroust, S. Hemmati, A. Ahmadi, E. Falletta, B. Ramavandi, C.L. Bianchi, Zn²⁺ removal from the aqueous environment using a polydopamine/hydroxyapatite/Fe₃O₄ magnetic composite under ultrasonic waves, *RSC Adv.* 11 (2021) 27309–27321.
- [58] L. Zhang, Z. Yang, W. He, J. Ren, C.Y. Wong, One-pot synthesis of a self-reinforcing cascade bioreactor for combined photodynamic/chemodynamic/starvation therapy, *J. Colloid Interface Sci.* 599 (2021) 543.
- [59] Y.N. Hao, A.Q. Zheng, T.T. Guo, Y. Shu, J.H. Wang, O. Johnson, W. Chen, Glutathione triggered degradation of polydopamine to facilitate controlled drug release for synergic combinational cancer treatment, *J. Mater. Chem. B* 7 (2019) 6742.
- [60] Y.H. Chen, I.J. Liu, T.C. Lin, M.C. Tsai, S.H. Hu, T.C. Hsu, Y.T. Wu, B.S. Tzang, W. H. Chiang, PEGylated chitosan-coated nanophotosensitizers for effective cancer treatment by photothermal-photodynamic therapy combined with glutathione depletion, *Int. J. Biol. Macromol.* 266 (2024) 131359.
- [61] Y.N. Wang, D. Song, W.S. Zhang, Z.R. Xu, Enhanced chemodynamic therapy at weak acidic pH based on g-C₃N₄-supported hemin/Au nanoplatfor and cell apoptosis monitoring during treatment, *Colloids Surf. B: Biointerfaces* 197 (2021) 111437.
- [62] C. Du, L. Zhou, J. Qian, M. He, Z.G. Zhang, C. Feng, Y. Zhang, R. Zhang, C.M. Dong, Ultrasmall zwitterionic polypeptide-coordinated nanohybrids for highly efficient cancer photothermal ferrotherapy, *ACS Appl Mater Interfaces* 13 (2021) 44002.
- [63] G. Huang, H. Huang, Hyaluronic acid-based biopharmaceutical delivery and tumor-targeted drug delivery system, *J. Control. Release.* 278 (2018) 122.
- [64] Y. Liu, C. Zhou, S. Wei, T. Yang, Y. Lan, A. Cao, J. Yang, Y. Hou, Paclitaxel delivered by CD44 receptor-targeting and endosomal pH sensitive dual functionalized hyaluronic acid micelles for multidrug resistance reversion, *Colloids Surf. B Biointerfaces* 170 (2018) 330.
- [65] R.J. Ju, L.M. Mu, W.L. Lu, Targeting drug delivery systems for circumventing multidrug resistance of cancers, *Ther. Deliv.* 4 (2013) 667.
- [66] R. Chang, Q. Zou, L. Zhao, Y. Liu, R. Xing, X. Yan, Amino-acid-encoded supramolecular photothermal nanomedicine for enhanced cancer therapy, *Adv. Mater.* 34 (2022) 2200139.
- [67] R. Cao, W. Sun, Z. Zhang, X. Li, J. Du, J. Fan, X. Peng, Protein nanoparticles containing Cu(II) and DOX for efficient chemodynamic therapy via self-generation of H₂O₂, *Chin. Chem. Lett.* 31 (2020) 3127.
- [68] S.Y. Kim, S.J. Kim, B.J. Kim, S.Y. Rah, S.M. Chung, M.J. Im, U.H. Kim, Doxorubicin-induced reactive oxygen species generation and intracellular Ca²⁺ increase are reciprocally modulated in rat cardiomyocytes, *Exp. Mol. Med.* 38 (2006) 535.
- [69] Z. Zhang, D. Ding, J. Liu, C. Huang, W. Li, K. Lu, N. Cheng, Supramolecular nanozyme system based on polydopamine and polyoxometalate for photothermal-enhanced multi-enzyme cascade catalytic tumor therapy, *ACS Appl. Mater. Interfaces* 15 (2023) 38214.
- [70] X. Lin, H. Chen, T. Deng, B. Cai, Y. Xia, L. Xie, H. Wang, C. Huang, Improved immune response for colorectal cancer therapy triggered by multifunctional nanocomposites with self-amplifying antitumor ferroptosis, *ACS Appl. Mater. Interfaces.* 16 (2024) 13481.
- [71] M.Y. Shen, T.I. Liu, T.W. Yu, R. Kv, W.H. Chiang, Y.C. Tsai, H.H. Chen, S.C. Lin, H. C. Chiu, Hierarchically targetable polysaccharide-coated solid lipid nanoparticles

- as an oral chemo/thermotherapy delivery system for local treatment of colon cancer, *Biomaterials* 197 (2019) 86.
- [72] L. Sivak, V. Subr, J. Tomala, B. Rihova, J. Strohalm, T. Etrych, M. Kovar, Overcoming multidrug resistance via simultaneous delivery of cytostatic drug and P-glycoprotein inhibitor to cancer cells by HPMA copolymer conjugate, *Biomaterials* 115 (2017) 65–80.
- [73] L. Ke, F. Wei, L. Xie, J. Karges, Y. Chen, L. Ji, H. Chao, A biodegradable iridium(III) coordination polymer for enhanced two-photon photodynamic therapy using an apoptosis-ferroptosis hybrid pathway, *Angew. Chem. Int. Ed.* 61 (2022) 202205429.
- [74] Z. Yang, N. Sun, R. Cheng, C. Zhao, Z. Liu, X. Li, J. Liu, Z. Tian, pH multistage responsive micellar system with charge-switch and PEG layer detachment for co-delivery of paclitaxel and curcumin to synergistically eliminate breast cancer stem cells, *Biomaterials* 147 (2017) 53.
- [75] R. Xing, Q. Zou, C. Yuan, L. Zhao, R. Chang, X. Yan, Self-assembling endogenous biliverdin as a versatile near-infrared photothermal nanoagent for cancer theranostics, *Adv. Mater.* 31 (2019) 1900822.
- [76] S. Li, R. Chang, L. Zhao, R. Xing, J.C.M. van Hest, X. Yan, Two-photon nanoprobe based on bioorganic nanoarchitectonics with a photo-oxidation enhanced emission mechanism, *Nat. Commun.* 14 (2023) 5227.